Geochemistry, Geophysics, Geosystems®

AGU ADVANCING EARTH AND SPACE SCIENCE

RESEARCH ARTICLE
10.1029/2021GC010325

D'' Reflection Polarities Inform Lowermost Mantle Mineralogy

C. Thomas[1], L. J. Cobden[2], and A. R. T. Jonkers[1]

[1]Institut für Geophysik, Westfälische Wilhelms-Universität Münster, Münster, Germany, [2]Department of Earth Sciences, Universiteit Utrecht, Utrecht, The Netherlands

Key Points:

- Ratio (*R*) of *S*- over *P* wave velocity changes (%) controls the polarity of *P* wave reflections at D'' reflector
- Thermochemical modeling and statistical analysis show specific minerals contributing to large *R*-values
- Polarity observations indicate that part of the Pacific large low seismic velocity province is due to bridgmanite enrichment

Supporting Information:

Supporting Information may be found in the online version of this article.

Correspondence to:

C. Thomas,
cthom_01@uni-muenster.de

Citation:

Thomas, C., Cobden, L. J., & Jonkers, A. R. T. (2022). D'' reflection polarities inform lowermost mantle mineralogy. *Geochemistry, Geophysics, Geosystems*, *23*, e2021GC010325. https://doi.org/10.1029/2021GC010325

Received 4 JAN 2022
Accepted 23 AUG 2022

Author Contributions:

Conceptualization: C. Thomas
Formal analysis: L. J. Cobden
Funding acquisition: C. Thomas
Investigation: C. Thomas
Methodology: C. Thomas, L. J. Cobden, A. R. T. Jonkers
Project Administration: C. Thomas
Software: A. R. T. Jonkers
Validation: C. Thomas, A. R. T. Jonkers
Visualization: C. Thomas, A. R. T. Jonkers
Writing – original draft: C. Thomas, L. J. Cobden, A. R. T. Jonkers

Abstract Polarities of seismic reflections at the discontinuity atop the D'' region (PdP and SdS) indicate the sign of the velocity contrast across the D'' reflector. Recent studies found PdP polarities matching and opposite those of *P* and PcP. While anisotropy could explain this behavior, we find that the ratio of the change in *S* wave velocity over change in *P* wave velocity (*R*-value) can influence polarity behavior of D'' reflected *P* waves. For *R*-values exceeding 3, the *P* wave reverses polarity in the absence of anisotropy while *S* wave polarity is not influenced by the *R*-value. Using sets of one million models for normal mantle and MORB with varying minerals and processes across the boundary, we carry out a statistical analysis (Linear Discriminant Analysis) finding that there is a marked difference in mantle mineralogy to explain *R*-values larger and smaller than 3, respectively. Based on our results we can attribute different mineralogy to a number of cases. In particular, we find that when velocities increase across D'' and polarities of PdP and SdS are opposite the post-perovskite phase transition is still the best explanation whereas MORB is the best explanation when PdP and SdS are the same. When the velocities are decreasing, the post-perovskite phase transition within MORB is the best explanation if PdP and SdS polarities are the same but if PdP and SdS are opposite, our results indicate that primordial material or mantle enriched in bridgmanite can explain the polarity behavior, further constraining mineralogy within the large low seismic velocity provinces.

Plain Language Summary Polarities of seismic waves reflecting at structures in the Earth's mantle indicate seismic velocity changes there. For the lowermost mantle reflector, a velocity increase generates a polarity that is the same for the main wave and the core-reflected wave. If, however, the percentage change of the velocity of the *S* wave increases at least three times as much as that of the *P* wave velocity (expressed as the *R*-value, the ratio d*Vs*/d*Vp*), the polarity of the D''-reflected PdP wave changes polarity, becoming opposite to both the main *P* wave and the reflection from the core-mantle boundary below it. Here, we analyze sets of 1 million models with variable compositions of mantle material and mid-ocean ridge basalt and use an advanced statistical method to identify those combinations of minerals that produce large positive *R*-values. We distinguish four cases and find that previous explanations for three of these cases concur with our analysis. For regions where velocities decrease over the D'' reflector, our analysis shows that enrichment with the lower-mantle mineral bridgmanite is responsible for the observed polarity behavior of *P* and *S* waves. This means that for regions such as large low-velocity anomalies in the lowermost mantle, primitive or bridgmanite-enriched material is the preferred explanation.

1. Introduction

The lowermost mantle of the Earth, the D'' region (Bullen, 1949), is characterized by a range of seismic structures that have been studied with a variety of seismic methods, in order to understand their formative processes and mineralogy in the deep Earth (for overviews, see Garnero, 2000; Lay, 2015). One prominent feature of the lowermost mantle is a seismic discontinuity at the top of the D'' region that generates reflections for *S* and *P* waves (see reviews by Cobden et al., 2015; Lay, 2015; Jackson & Thomas, 2021; Wysession et al., 1998). Several explanations for this reflector at the top of D'' have been discussed, such as subducted slabs (e.g., Lay & Garnero, 2004), scatterers (Scherbaum et al., 1997), and the post-perovskite phase transition (e.g., Murakami et al., 2004; Oganov & Ono, 2004; Shim, 2008; Tsuchiya et al., 2004).

The D'' reflector has been found in many regions at approximately 300 km above the CMB, constrained mostly by travel times of the reflected waves off the top of D'' (Cobden et al., 2015; Lay & Helmberger, 1983; Weber, 1993; Wysession et al., 1998) with depth variations of about ±100 km. But whereas in the past travel times of seismic

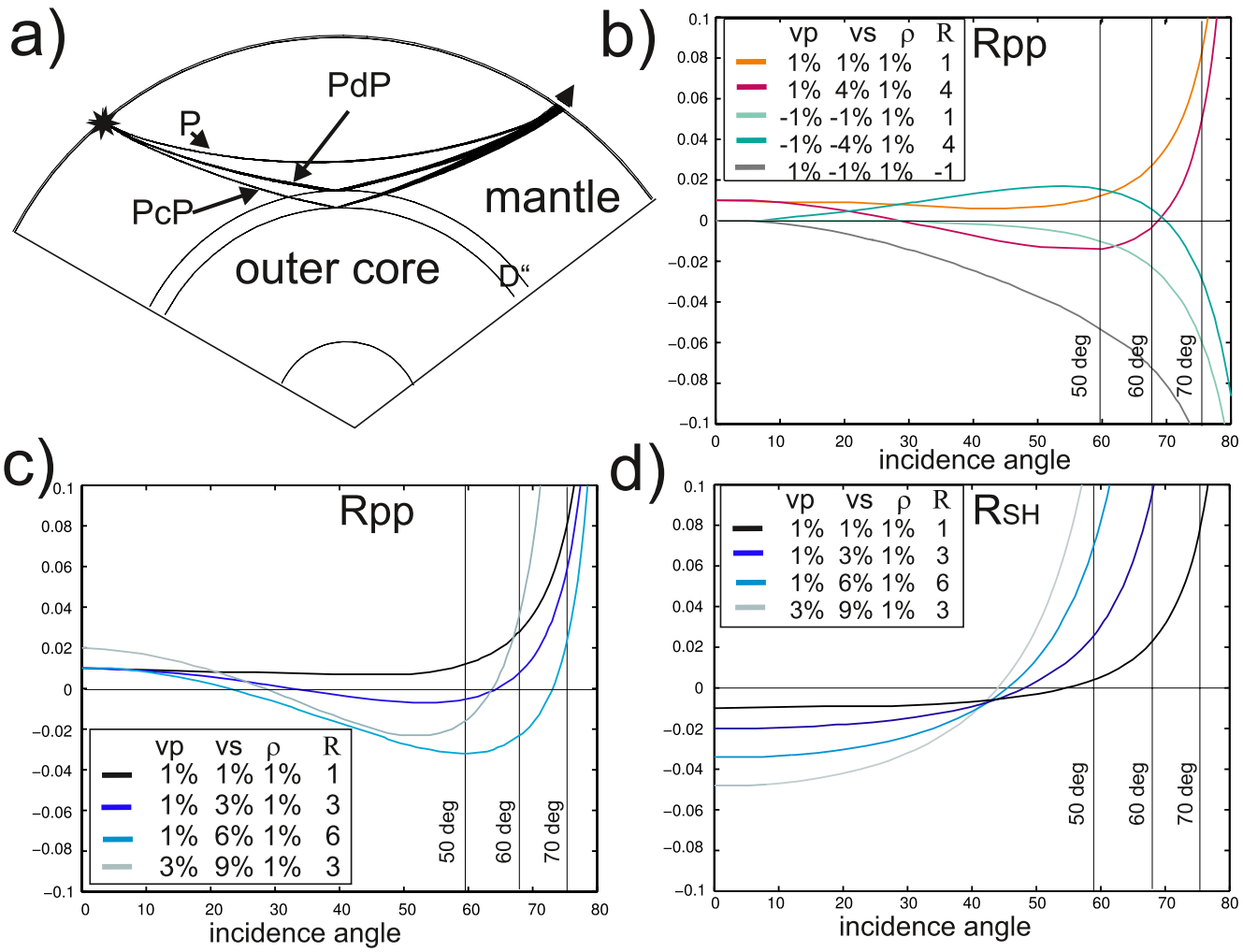

Figure 1. (a) Wave paths of *P* waves, the reflection off the D" discontinuity PdP, and PcP, the CMB-reflected phase. Same paths for *S*, SdS, and ScS. (b) Reflection coefficient for *P* to *P* reflections (Rpp) at the D" discontinuity with variable changes in *Vp*, *Vs* and density across the reflector as given in the legend. (c) Same as for (b) but for different (but only positive) values of the changes in *Vp* and *Vs* across D". (d) Same as (c) but for SH to SH reflection coefficient (RSH). The distance corresponding to the incidence angle at the discontinuity is given by the vertical lines in (b–d).

data were most commonly used for studying the reflector, recently wave amplitudes and polarities have also been used to extract details about D" structures (e.g., Cobden & Thomas, 2013; Pisconti et al., 2019; C. Thomas et al., 2011; Thorne et al., 2007). For example, complexity in waveforms can indicate layering (e.g., Moore et al., 2004; Rost et al., 2005; Schumacher et al., 2018; C. Thomas et al., 1998), and wave amplitude behavior has provided information on attenuation (e.g., Cormier, 1982; Lay & Helmberger, 1981) or gradients of seismic reflectors in the Earth (e.g., Lay, 2008; Weber, 1993). In addition, polarities of seismic waves can provide information about velocity and density variations, that is, the impedance contrast, across a reflector (Zoeppritz, 1919).

Previous work on D" reflections (e.g., Cobden & Thomas, 2013; Cobden et al., 2015; Lay & Helmberger, 1983; Weber, 1993) has shown that the polarities of these reflected *P* or *S* waves correlate with the velocity jump across the reflector. This means that for a *P* wave velocity increase across D", the reflection off this layer (PdP, see Figure 1a) will show the same polarity as both the direct *P* wave traveling above it and PcP, the *P* wave reflection off the core-mantle boundary (CMB). The same is true for *S* waves. Lay et al. (2004) stated that the density has little influence on amplitudes of the reflected waves at epicentral distances exceeding 60°, therefore models have often been calculated based only on the change in *Vp* and *Vs* (e.g., Lay & Helmberger, 1983; Weber, 1993; Young & Lay, 1990). The magnitude of the velocity jump is generally determined by comparing the observed amplitude of the reflected wave with synthetic predictions, often using 1D modeling (e.g., Lay & Helmberger, 1983;

Weber, 1993). The estimated wave-velocity jumps usually range from 1% to 3%, but can occasionally reach 5% (Bréger & Romanowicz, 1998; C. Thomas & Laske, 2015).

Interestingly, recent observations of PdP-wave polarities have in some cases shown opposite polarities to PcP- and *P* waves (e.g., Hutko et al., 2008; Pisconti et al., 2019; C. Thomas et al., 2011), which would suggest a seismic velocity reduction across the reflector, while SdS waves in these regions show polarities that agree with *S* and ScS, indicating a positive velocity jump across D" (e.g., Chaloner et al., 2009; Cobden & Thomas, 2013; C. Thomas & Laske, 2015). This discrepancy between PdP and SdS polarities excludes a purely thermal origin, since one would expect both velocities to increase given a temperature reduction. The mineral phase transition of bridgmanite to post-perovskite in $MgSiO_3$ (Murakami et al., 2004; Oganov & Ono, 2004; Shim et al., 2004; Tsuchiya et al., 2004), which occurs near the CMB, has been shown in theoretical mineral physics calculations to be potentially associated with a small change in *P* wave-velocity (which can be either positive or negative) and a larger increase (of up to 3%) in *S* wave-velocities (Wookey et al., 2005; Tsuchiya & Tsuchiya, 2006; Wentzcovitch et al., 2006; for a compilation of published wave velocity changes in D" related to the post-perovskite phase transition, see Cobden et al., 2015). Hence the presence of post-perovskite could potentially explain these discrepant PdP- and SdS polarity observations. In other regions, however, the PdP wave exhibits the same polarity as *P* and PcP, while SdS also shows the same polarity as *S* and ScS (Cobden & Thomas, 2013; Thomas & Weber, 1997; Weber, 1993). This would make pure $MgSiO_3$ post-perovskite (Wookey et al., 2005) an unlikely explanation for the D" reflector in those places (e.g., Cobden & Thomas, 2013), but the latter could still be caused by post-perovskite if the *P* wave velocity change is positive across the phase transition (e.g., Tsuchiya & Tsuchiya, 2006).

It has been shown (Pisconti et al., 2019; C. Thomas et al., 2011) that in some areas *P* wave polarity depends on the direction of wave propagation (i.e., azimuth) and that deformation, that is, anisotropy in D", can change the polarity of *P* waves and potentially also *S* waves (Creasy et al., 2019; Pisconti et al., 2019; C. Thomas et al., 2011). To our knowledge, array observations of SdS waves with an opposite polarity to *S* and ScS have not been reported, but stacks of seismic data (e.g., Lay et al., 2006) and inversions (Kawai & Geller, 2010; Konishi et al., 2009) suggest that velocity decreases for *S* waves also exist. Using azimuthal as well as distance dependence of the polarities of *P* and *S* wave D" reflections can help to further constrain mineralogy in D" (Creasy et al., 2019; Pisconti et al., 2019).

Most aforementioned observations have been made in regions where tomographic inversions suggest above-average velocities (Hosseini et al., 2018, 2020; Li et al., 2008; Ritsema et al., 2011). If deep subduction is responsible for the D" reflector in these cases, a post-perovskite phase transition would be a good explanation, since post-perovskite would preferably be found in colder mantle regions (e.g., Cobden & Thomas, 2013; Cobden et al., 2015; Hernlund et al., 2005). Moreover, this would also agree with the mineralogical best fit for anisotropy in post-perovskite (Creasy et al., 2019; Pisconti et al., 2019; Romanowicz & Wenk, 2017; C. Thomas et al., 2011).

For regions associated with below-average wave speeds, it has been suggested that observations of PdP and SdS reflections may not be due to a simple Mg-bridgmanite to post-perovskite phase transition, due to the positive Clapeyron slope of the phase transition (Murakami et al., 2004; Oganov & Ono, 2004), and the possibility that slower-than-average regions may be warmer (e.g., Hernlund et al., 2005). However, when this phase transition takes place in Fe- and Al-bearing bridgmanite, or in a multi-mineral assemblage, then the depth and strength of the discontinuity can change, as well as introducing a broad depth interval over which the transition occurs (e.g., Catalli et al., 2009; Cobden et al., 2015; Grocholski et al., 2012; Hernlund, 2010; Kuwayama et al., 2022), even moving the phase transition to pressures inside the core. A broad phase transition region may make observations of the seismic reflector off this phase transition more difficult to observe since it results in small amplitudes of D" reflected waves. Interestingly, in some of these low-velocity regions, *P* (and *S*, respectively) wave reflections off D" show the same polarity as the direct *P* wave (*S*) and core reflected PcP wave (ScS). This indicates an increase in seismic wave velocity across D", even though a tomographic model might suggest slow wave velocities regionally, which would lead to an opposite polarity for a reflection from these regions (e.g., Cobden & Thomas, 2013; Jackson & Thomas, 2021). However, one should be cautious when comparing D" reflection points with tomographic models in detail, since the latter is concerned with large-scale lateral variations in wave velocity, and a lack of model resolution and other uncertainties limit the interpretation of structures at the relatively small length scale of D" reflection points. Also, lateral homogeneity in a tomography model does not preclude vertical changes in wave velocity.

In summary, polarity observations of *P* and *S* waves reflecting off the D" region seem variable, and while anisotropy could potentially explain these variations, here we investigate whether an alternative explanation could also produce polarity changes of D" reflections.

2. Modeling of Polarities

The reflection coefficient is controlled by the impedance contrast (density × velocity) for *P* and *S* waves across a discontinuity, and the angle of incidence of the wave at the discontinuity (Zoeppritz, 1919, see also descriptions and approximations in Aki and Richards, 1980; Bortfeld, 1961). The amplitudes of reflected and transmitted waves for an incoming *P* or *S* wave are governed by the velocities of *P* and *S* waves, by density (impedance) contrasts and also ratios of *P* and *S* wave velocities above and below the boundary. For a reflection off the top of the discontinuity, the reflection coefficient will, for sufficiently large angles of incidence, enter the overcritical range (e.g., Weber, 1993), causing a phase change and strongly enhancing the amplitude of the reflection (see Figures 1b–1d). For this reason, most previous D" reflection studies favor a distance range of 65°–85° (e.g., Cobden et al., 2015; Lay, 2015; Wysession et al., 1998 for reviews) to benefit from large amplitudes.

To investigate polarities of D" reflections (PdP and SdS, Figure 1a), we vary *P* and *S* wave velocity jumps (d*Vp* and d*Vs*) as well as the density jump across the boundary, and compute the reflection coefficient for *P* and SH wave reflections. We verify the results using three different methods (Reflectivity method, Müller, 1985; Zoeppritz explorer (Crewes Explorer Programs, 2022) and Javascript solver for Zoeppritz equations (Frederiksen, 2022). For completeness, we also tested converted waves (PdS and SdP waves) and SV reflections, although those have not been used extensively for D" studies. We express the velocity changes of *Vp* and *Vs* through the (R)atio of percent *Vs* change over percent *Vp* change, the so-called *R*-value (similar to the concept of *R* in seismic tomography, e.g., Karato & Karki, 2001; Koelemeijer et al., 2016; Masters et al., 2000). Thus a 1% change in *Vp* in combination with a 3% change in *Vs* would yield an *R*-value of 3.

We confirm that for the distance ranges often used for D" reflection observations (65°–85° distance), which correspond to incidence angles above 70° (Figures 1b–1d), a velocity increase in *Vp* produces the same polarity as that of *P* and PcP (and ditto for *S* waves). However, we find that from an *R*-value of 3, which means that the %-change of *Vs* is at least 3 times that of the %-change of *Vp*, the reflection coefficient for the *P* wave becomes negative for part of the incidence angle range (Figures 1b and 1c). The size of the reflection coefficient increases with increasing *P* wave velocity jump (blue and gray lines compared with black line in Figure 1c), but the *R*-value determines whether for part of the incidence angle range the *P* wave reflection coefficient becomes smaller than zero, resulting in a PdP wave polarity opposite to that of *P* and PcP (black line vs. blue and gray lines in Figure 1c). The same is true for *P* wave reflection coefficients for negative *Vp* and negative *Vs* changes (Figure 1b).

However, if either *Vp* or *Vs* increases while the other velocity decreases, this effect does not occur. Taking the case of a small *P* wave velocity reduction with an *S* wave velocity increase (negative *R*-value, dark gray line in Figure 1b), as is expected for the bridgmanite to post-perovskite phase transition in $MgSiO_3$ (e.g., Wookey et al., 2005), this yields a PdP-wave polarity opposite to that of *P* waves, as expected for velocity reductions, but no polarity change over the entire incidence angle range occurs for all *R*-values. But such a case of opposite changes for *P* and *S* wave contrasts causes amplitudes to be slightly larger than for changes with the same sign (see also Cobden et al., 2015).

Due to the reflection coefficient becoming negative for part of the incidence angle range, as shown in Figures 1b–1d, the reflection coefficient also has up to two angles (Brewster angles, in analogy to optics, Červený, 2001; Tatham & Krail, 2012; Yang et al., 2021) where no *P* wave is reflected in case of an incident *P* wave. The same is true for an incident *S* wave, however, only one Brewster angle is usually found there (e.g., Müller, 2007; Červený, 2001). Waves do behave non-intuitively at interfaces (see also Malcolm & Trampert, 2011; Sollberger et al., 2018), so it is not straightforward to explain the physical reason behind the behavior of reflection coefficients, but it is likely that it arises due to the interaction (and production) of the SV wave at the interface, as well as the reflected and transmitted *P* wave, together with the relevant boundary conditions (Červený, 2001).

Looking at the SH-wave reflection coefficient, we find that an *R*-value smaller or larger than 3 does not affect the polarity of the *S* wave reflection much in the distance range used for observing D" reflections; it mostly changes the amplitude of the wave (Figure 1d) and, to a small degree, the incidence angle at which the polarity change

occurs, which always happens for the *S* wave reflection coefficient (e.g., Müller, 2007). The *S* wave reflection coefficient shows a polarity change for incidence angles smaller than 50°, which translates into small epicentral distances (<40°–45°, depending on *P* and *S* velocity changes, see Figure 1d), so usually it is not tested for D" studies. For the larger epicentral distances often used in D" studies (i.e., 65° and above), the SdS-wave will therefore always show a polarity that is the same as the *S* wave for velocity increases. We also found that that PdS and SdP waves and vertically polarised SdS waves show no change in polarity with varying *R*-values, only a change in the size of the reflection coefficient, leading to amplitude changes of the waves. Thus, we concentrate in the following on the polarity behavior of PdP waves only.

So far, we have only looked at changes in *Vp* and *Vs*. Lay et al. (2004) mention that the density has little effect on the amplitude of the reflected wave and therefore on the reflection coefficient for epicentral distances of 70° and larger, and in our studies this is indeed the case, even for large *R*-values. Regarding smaller distances, the change in density does not influence the incidence angle at which the reflection coefficient changes polarity, but it does affect the amplitude of the wave at short incidence angles, that is, at distances below 10°–20°.

For *R*-values of 3 and 4, the epicentral distance that corresponds to the incidence angle at which the PdP wave reverses polarity is smaller than that used in most studies, and only short-distance data of 40°–65° would allow detection of this reflection coefficient polarity behavior (Figure 1b). Few observed steep-angle D" reflections have been reported so far (e.g., Schimmel & Paulssen, 1996 [using *S* waves], C. Thomas & Laske, 2015 [using *P* waves]), mostly because the amplitudes are so small that the reflections have to be detected using stacking methods (e.g., Cobden & Thomas, 2013; Kito et al., 2007; C. Thomas, Garnero, & Lay, 2004; C. Thomas, Kendall, & Lowman, 2004; Weber, 1993). Increasing the size of the *R*-value shifts the transition from a negative to a positive reflection coefficient (i.e., from opposite to same polarity of PdP with respect to *P*) to larger epicentral distances, allowing this behavior to also be observed at larger distances; however, very large *R*-values ($R > 5$) may be unrealistic for the Earth.

The behavior of the reflection coefficient allows us to test the ratio of changes in *P*-velocity vs. *S* velocity, which may help to constrain the mineralogy of the D" region and the cause for the observed D" reflector. But because the reflection coefficient is very small, it is necessary to test whether a D" reflection would still be visible in seismic data. To confirm our reflection coefficient findings, we use the reflectivity method (Müller, 1985) to generate synthetic data for *R*-values larger and smaller than 3. Since PdP arrivals are usually small in a seismogram, we generate fourth root vespagrams (e.g., Davies et al., 1971; Muirhead & Datt, 1976; Rost & Thomas, 2002; Schweitzer et al., 2002) in which these arrivals can be detected and distinguished by their slowness values. Vespagram processing has been used in many studies to detect *P* and *S* wave reflections off the D" discontinuity (e.g., Cobden & Thomas, 2013; Kito et al., 2007; Pisconti et al., 2019; C. Thomas, Garnero, & Lay, 2004; C. Thomas, Kendall, & Lowman, 2004; C. Thomas & Weber, 1997; Weber, 1993). Figure 2a shows an example vespagram for synthetic data generated by a model with a velocity increase across D" and an *R*-value of 2. Contrastingly, Figure 2b shows a vespagram for a model with a velocity increase across D" and an *R*-value of 6. The inset shows the PdP wave; one can clearly see that the polarity of PdP of Figure 2b is opposite to that of *P* and PcP, while in Figure 2a the PdP polarity is the same as that of *P* and PcP. The vespagrams are generated for stations in an epicentral distance of 45°–52°. To demonstrate that the change in polarity is distance-dependent, Figure 3 shows the traces for 62° and 48° for the case of an *R*-value of 1 (black curve) and an *R*-value of 4 (red curve). The wave at 48° arriving at 52 s is the depth phase pP, which can be distinguished by its slowness in the vespagram in Figure 2.

3. Comparison With Data

Our modeling shows that an observation of the effect of *R*-values larger than 3 on seismic polarities is theoretically possible. We searched the literature for evidence of published *R*-values greater than 3 in the lower mantle, but found most published velocity ratios for the D" region in the range of 1–3, where a ratio of 3 is often interpreted as melt (Dobrosavljevic et al., 2019; Jackson & Thomas, 2021; Rost et al., 2005; Williams & Garnero, 1996). Tomographic inversions show *R*-values ($d\ln Vs/d\ln Vp$ in this case) of up to 5 in the lowermost mantle (Koelemeijer et al., 2016, 2018) and even higher (Cobden et al., 2012). Mineralogically, *R*-values larger than 3 are possible (Cobden et al., 2012; Deschamps & Trampert, 2003; Hernlund & Houser, 2008; Karato & Karki, 2001) and should generate polarity reversals for part of the distance range. In fact, high *P-T* experiments

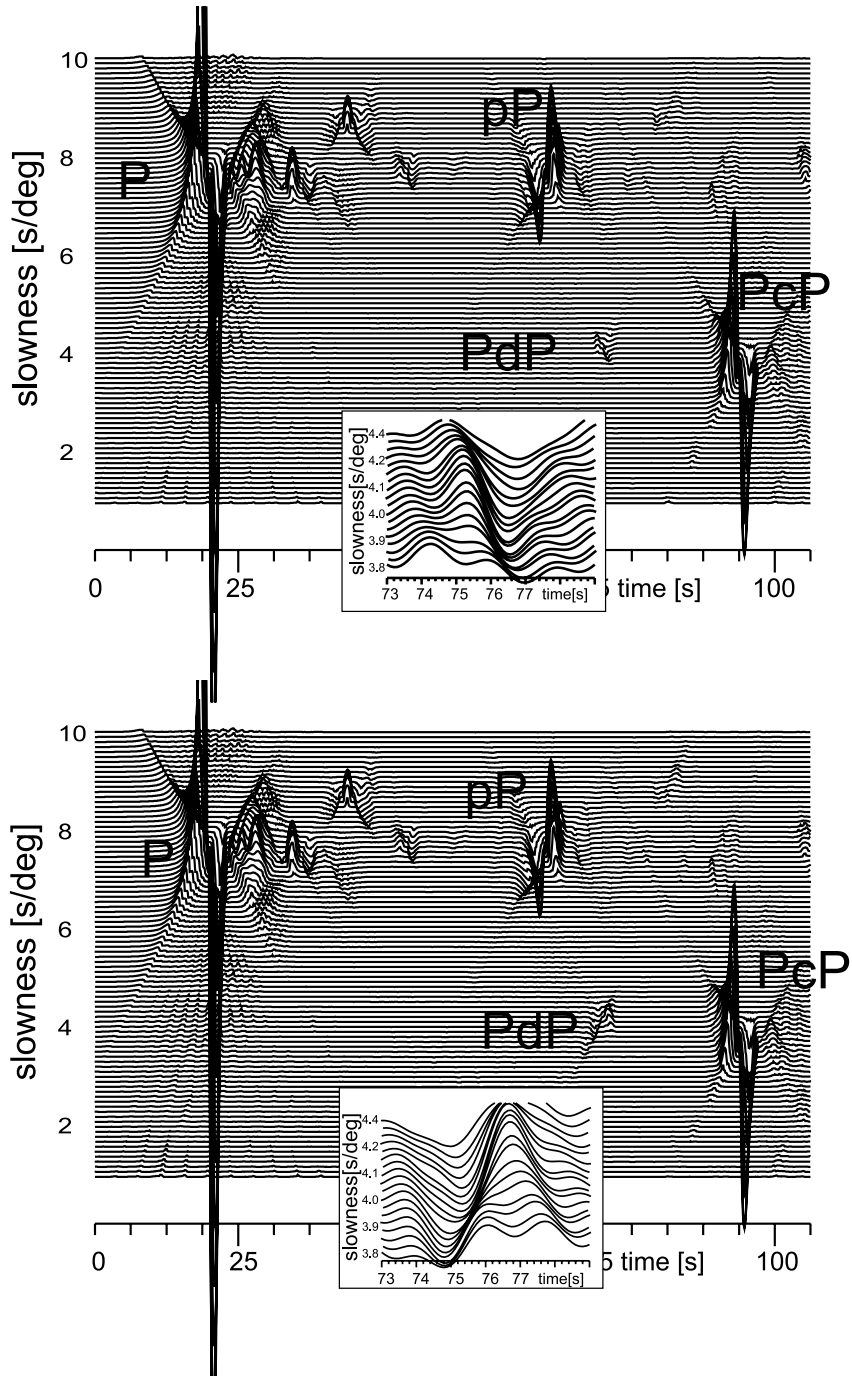

Figure 2. Fourth root vespagrams for two synthetic data examples: top: an *R*-value of 2, bottom: an *R*-value of 6. The insets show the PdP wave for a better comparison with *P* and PcP waveforms and polarities. The arrival at 75 s with *P*-slowness is the pP wave.

suggest that for Fe-rich (Mg, Fe)O, the *R*-value could be up to 6–9 if Reuss-bound mixing models are employed (e.g., Dobrosavljevic et al., 2019). It is therefore necessary to assess the polarity of PdP waves at short distances in real data, to verify our modeling results.

Most PdP wave reflections have been detected for large epicentral distances (larger 60°) and cases of opposite as well as the same PdP polarity compared with the main phases (PcP and *P*) have been found. In contrast, most SdS reflections seem to have the same polarity as ScS and *S*, except for the Pacific (Lay et al., 2006; Ohta et al., 2008).

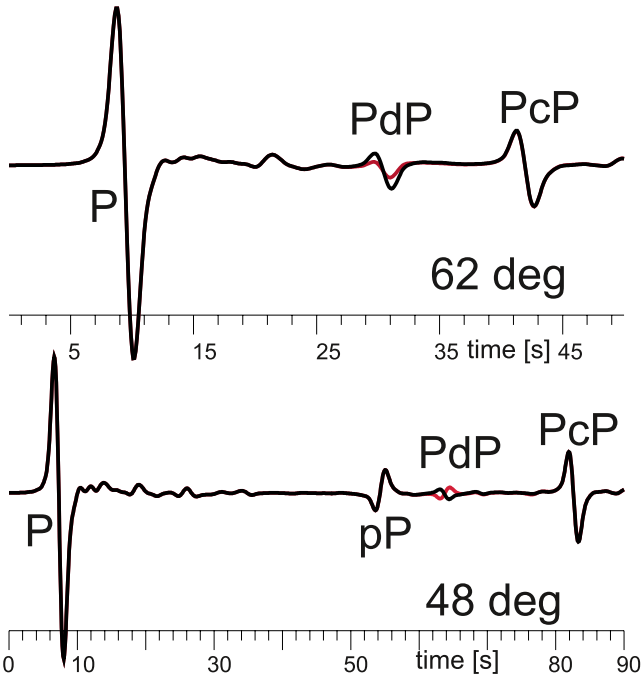

Figure 3. Seismogram section for the model with *R*-value of 2 (black line) and *R*-value of 6 (red line) for two different distances, indicating the distance dependency of the polarity reversal. The *P* and PcP waves are clearly visible in both examples, the arrival at 52 s in the seismogram for 48° is the pP wave.

An overview of previously observed polarities for PdP waves can be found in Cobden and Thomas (2013) or Cobden et al. (2015). A recent study (Pisconti et al., 2019) detected PdP and SdS waves beneath the Central Atlantic near the edge of the large velocity anomaly beneath Africa. In their work, the PdP waves for shorter distances showed opposite polarities with respect to *P*, while the SdS-waves had the same polarity as *S* for all distances. This polarity behavior is possible for an *R*-value exceeding 3, but is more likely for an *R*-value of about 5, since the angle of incidence at which the polarity changes sign (Figure 1) occurs at larger epicentral distances for $R = 5$ than for $R = 3$. Pisconti et al. (2019) showed that deformation of post-perovskite, that is, anisotropy, could be responsible for those variations in polarity of PdP, especially since they also used splitting measurements for the same region. It would be of interest to investigate a crossing path for this particular region to test their interpretation of anisotropy vs. the possibility of large *R*-values.

To examine other locations, we collected data from a number of seismic arrays to find D" reflections at short distances (between 40° and 60°) where we would expect a change in polarity of PdP if the *R*-value is larger than 3. Despite a large number of source-receiver combinations, we found only a small number of events that show an additional arrival in vespagram analysis (e.g., Rost & Thomas, 2002; Schweitzer et al., 2002) with a slowness and travel time that agree with a D" reflection. Since reflection coefficients for the selected distance range of 40°–60° are small (Figure 1), the reflection is often very small in the vespagram or might be buried in noise. Nevertheless, we were able to find a few cases where the polarity of the D" reflection can be extracted and compared with PcP and *P* (Figure 4). We verify that the D" reflections travel in plane by performing slowness-backazimuth analyses, as shown for one example event in Figure S1 in Supporting Information S1. It is possible that reflections that travel out-of-plane could arrive with an opposite polarity due to the radiation pattern or reflections at different structures, that is, not D" (Rochira et al., 2022; Schumacher & Thomas, 2016; Schumacher et al., 2018), therefore, in our study, we ensure that all waves travel in plane.

Two examples of D" reflections shown are from events in the Mariana region, detected at an array in Tibet (Tables S1 and S2 in Supporting Information S1), for which the distances are 49° and 51°. One of these D" reflections, located beneath the western Pacific, shows a polarity that is the same as PcP and *P* (Figures 4a and 4d), while the other shows an opposite polarity (Figures 4b and 4e). The region in D" where these two events reflect is associated with high to average *P* wave velocities in most tomographic models (e.g., Hosseini et al., 2020; Simmons et al., 2010), or a change from high to low-velocity as shown in Figure 4g for the tomographic model of Li et al. (2008). The third data example in Figure 4 is an event in Chile recorded at the Transportable Array (TA) stations in Kentucky (Tables S1 and S2 in Supporting Information S1), with an epicentral distance of 62°. The vespagram of this event shows a reflection with the same polarity as *P* and PcP (Figures 4c and 4f). This event is reflecting in an area characterized by past subduction (Figure 4h), and tomographic inversions for *P* waves show mostly fast velocities here (e.g., Hosseini et al., 2020; Li et al., 2008; Simmons et al., 2010).

We also re-examined some of the events from C. Thomas and Laske (2015), who used Ocean Bottom Seismometer (OBS) data of instruments installed around Hawaii, and detected PdP waves at short distances (Tables S1 and S2 in Supporting Information S1). These data suffered from noise: however, the polarity of the few events where a D" reflection could be determined, was often the same as PcP and *P*. Several of the source-receiver combinations were reflected from tomographically fast regions (see C. Thomas & Laske, 2015) where we might expect the same polarity of PdP compared with *P* and PcP, but some slow regions were also tested, and the reflections there also showed the same polarity for PdP compared with *P* and PcP. Figure 5a shows the vespagram for one event where the PdP polarity is clearly visible and is the same as the *P* and PcP wave. The D" reflection point for this event is in the large low seismic velocity province (LLSVP) as outlined in the *P* wave tomography by Li et al. (2008) in Figure 5b. The data for the other two reflection points of the events presented in C. Thomas and Laske (2015) that reflect nearby (Figure 5b) also show a polarity of PdP matching those of PcP and *P*.

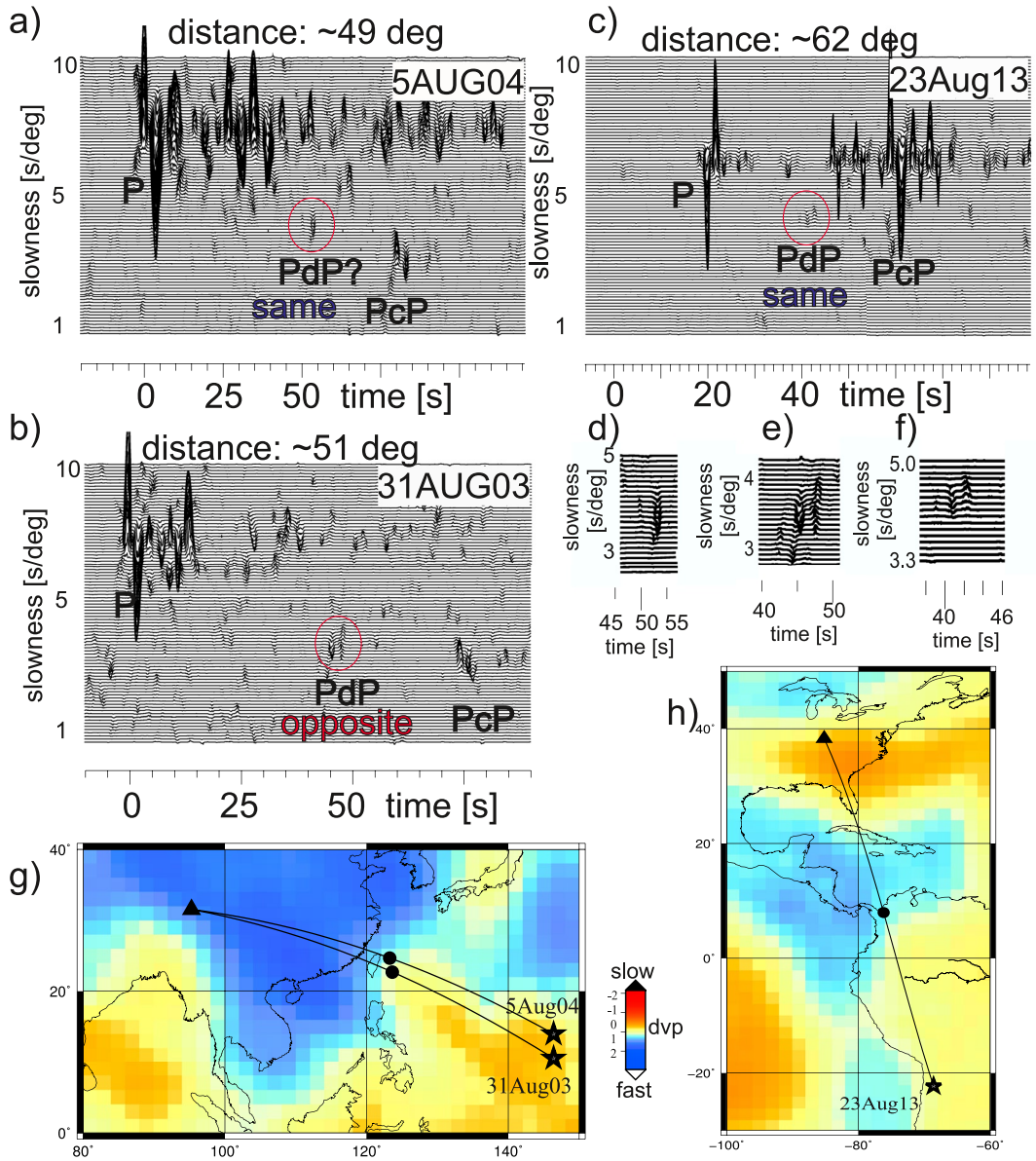

Figure 4. Three examples for fourth root vespagrams showing PdP (circled in red) at short distances. The distance to the central station is given above the vespagrams. (a) Event 5 August 2004 recorded at the array in Tibet, (b) event 31 August 2003 recorded at the array in Tibet, and (c) event 23 August 2013 recorded at stations of the TA in Kentucky (Table S2 in Supporting Information S1). The polarities are indicated in each vespagram. (d–f) show insets around the PdP wave for events in (a–c). (g) Sources (stars), central station of the array (triangle), great circle path and reflection points (circles) superimposed on a tomographic model MITP08 (Li et al., 2008) for the events in (a and b). (h) Same as in (g) but for the event in (c).

Taking these new observations into account and looking at published D" reflections, we find that D" reflections for *P* waves show both positive and negative polarities, not necessarily related to the velocity variations in the mantle mapped by tomography. *S* wave reflections from the D" reflector in most regions show the same polarity as the main waves (*S* and ScS) except for the Pacific (Lay et al., 2006; Ohta et al., 2008). While anisotropy can explain some of this behavior (e.g., Pisconti et al., 2019; C. Thomas et al., 2011), large *R*-values can also be due to changes in mineralogy. We will explore this scenario here.

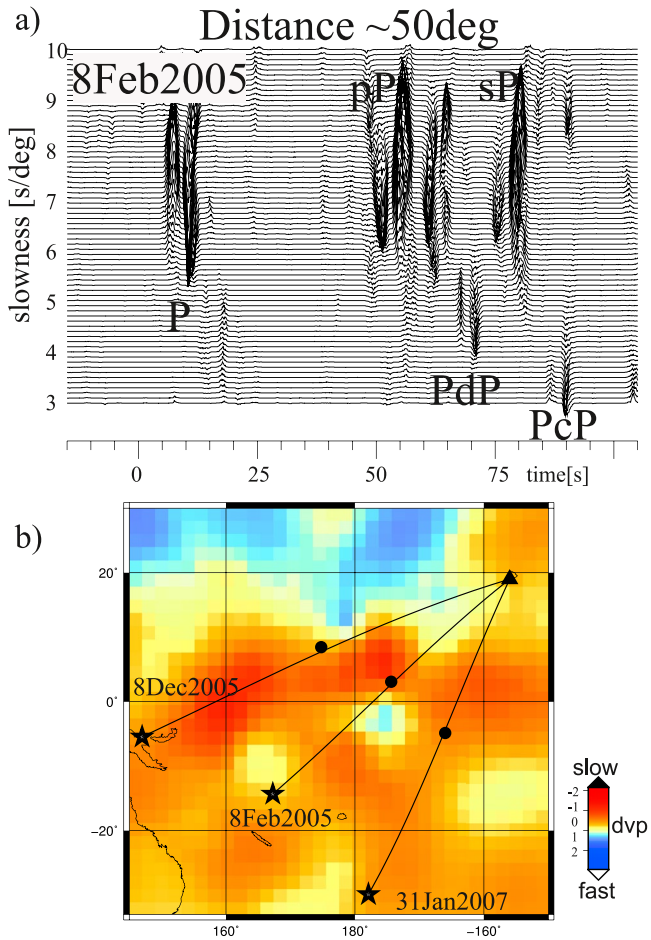

Figure 5. (a) As Figures 4a–4c but for event 8 February 2005 recorded at the PLUME array (Table S2 in Supporting Information S1). (b) As Figures 4f and 4g but for the event 8 February 2005. In addition, event locations and reflection points for 8 December 2005 and 31 January 2007 that were analyzed and shown in C. Thomas and Laske (2015) are also indicated.

Table 1
Ranges of the Thermochemical Parameters (Modeling Parameters) as Varied Between Models (Mantle Model)

Parameter	Minimum value	Maximum value
X. vol% (Mg, Fe) (SiO_3 + O)	85	100
Y. vol% (Mg, Fe) SiO_3 within X	60	100
Z. vol% $FeSiO_3$ within Y	0	20
K. Fe-Mg part. coeff bm-mw	0.0001	2.0
A. vol% $CaSiO_3$ within (100-X)	0	100
B. vol% SiO_2 within (100-X-A)	0	100
P. vol % bm and Al_2O_3 which converts to ppv	0	100
Temperature (K)	1,800	3,100

Note. See Supporting Information (Method 1) for explanation.

4. Thermochemical Models and Linear Discriminant Analysis (LDA)

To understand which parameters are most important in producing large *R*-values we re-analyzed the seismic properties of the thermo-chemical models presented in Cobden et al. (2012) and Cobden and Thomas (2013). The background to the models is explained in Methods 1 in the Supporting Information and the parameters are listed in Table 1. We call these models the Mantle simulation. In addition, we also tested models which include a layer of 100% MORB below the reflector, where post-perovskite is able to exist (see Supporting Information, Table S3 in Supporting Information S1). For each simulation, one million unique thermochemical models were produced.

In order to evaluate the *R*-values, we need to know the velocities and density of each model. First, bulk and shear moduli of the individual minerals were calculated from the elastic parameters published in Stixrude and Lithgow-Bertelloni (2011), using the equation of state in Stixrude and Lithgow-Bertelloni (2005). This involves a third order Birch-Murnaghan equation of state to calculate properties at high pressure, with a Mie Grüneisen correction for thermal pressure (Stixrude & Lithgow-Bertelloni, 2005). All calculations were performed at a pressure of 119 GPa, corresponding to a mantle depth of ~2,600 km. The *P* and *S* wave velocities of both starting (above D") and end (below D") model were then calculated from a Voigt-Reuss-Hill average of the bulk and shear moduli of the individual minerals, and a Voigt average of the density. We pinned the starting model above D" such that the velocities and density fall within 5% of 1D reference model ak135 (Kennett et al., 1995) to avoid extreme outliers. For each model run, we subtract the absolute percentages of the constituent minerals above the reflector from those below it, which yields the changes in composition downward across the boundary. We then evaluated the calculated wave velocities for each model, and performed a detailed analysis of those that produced a ratio of d*Vs*/d*Vp* of 3 and larger across the boundary.

Since one million models is too large a number to consider individually, we turned to LDA, a powerful statistical technique for classifying existing and new data into predefined discrete groups ("classes"). It is similar to Principal Component Analysis (PCA) in that it involves data reprojection into an eigenspace with useful properties; in this case: maximizing the separability of known classes while taking into account their internal (i.e., class-specific) variance. LDA is different from PCA in that the eigenvectors are based upon the between-class data scatter scaled by the within-class scatter (Martinez & Kak, 2001), rather than the data covariance used in PCA. The technique was first published by Fisher (1936, in Duda & Hart, 1973); for a recent treatment, see for example McLachlan (2005). Applying PCA instead would be unsuitable here, as the aim of this study is not to define abstract independent components (comprised of various positive or negative contributions from many inputs), but instead to identify predefined *R*-value-based classes in terms of specific combinations and regimes of the original modeling parameters.

Here, we use LDA as a class "filter" on the full data sets (of modeling and chemical composition parameters, respectively), in order to identify which original model parameters contribute most to class separability, more specifically in distinguishing between low- and high *R* regimes (i.e., below/above $R = +3$). That is, after LDA reprojection we reject those data that are misclassified in terms of those subsets, thereby reducing the error in the subsequent statistical significance assessment of the input parameters. We also only keep

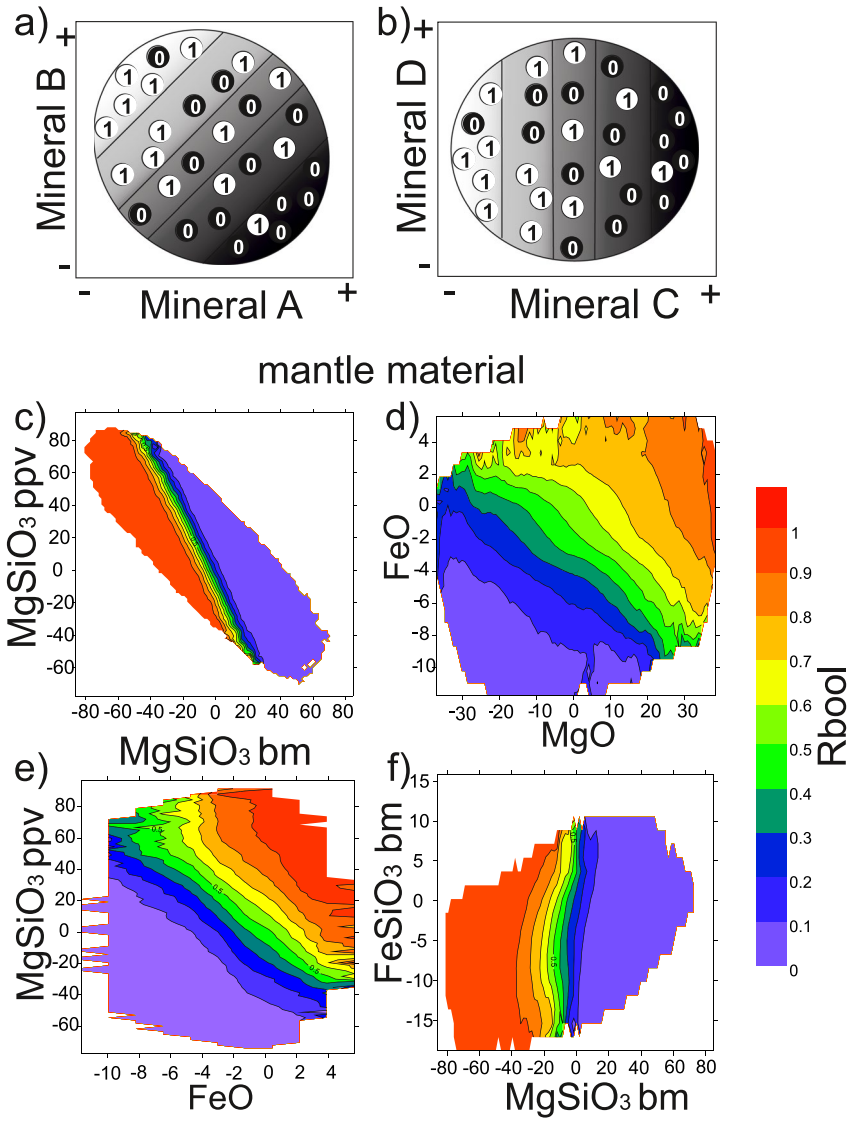

Figure 6. (a, b) Explanation for the following plots and the calculation of the local average Rbool, derived from the point cloud of correctly classified linear discriminant analysis (LDA) results containing an equal number of low- (0) and high-*R* cases (1). Black regions mean most values are 0, while in white regions most values are 1. (a) For the case that both mineral changes are important for generating large *R*-values (here decreasing A and increasing B percentages). (b) example of mineral C being important for generating large *R*-values but not mineral D. (c–f) Color coded Rbool (0, purple: low *R*-values, i.e., smaller than 3; 1, red: high *R*-value, i.e., 3 and above) for different combinations of minerals of mantle material (Table 1) as indicated on the diagrams for the case of both *Vp* and *Vs* increasing across the D" reflector.

cases for which $R > 1$ (see Method 2 in Supporting Information). The final objective is to construct balanced, distinct profiles of these parameters for low- and high *R*-values respectively, while distinguishing between two seismological cases: changes in *P* and *S* velocity being both positive, or both negative (both of which yield a positive *R*-value). A flow diagram of the process is shown in Figure S2 in Supporting Information S1. The relevant numbers for the data sets and more information on the LDA process are provided in Methods 2 in the Supporting Information and in Figure S3 in Supporting Information S1.

To simplify subsequent analysis and visualization of the results, we encoded the two *R* regimes in the LDA results as variable *Rbool*(ean), with 0 and 1 representing low and high *R* respectively. Whereas correctly classified LDA results are discrete, that is, either zero (low-*R*) or unity (high-*R*), Rbool is the continuous spatial average of a large number of these points, with equal numbers of low- and high-*R* cases, when plotted in multidimensional modeling parameter space (Figures 6a and 6b). Wherever low values dominate (black regions in Figures 6a and 6b,

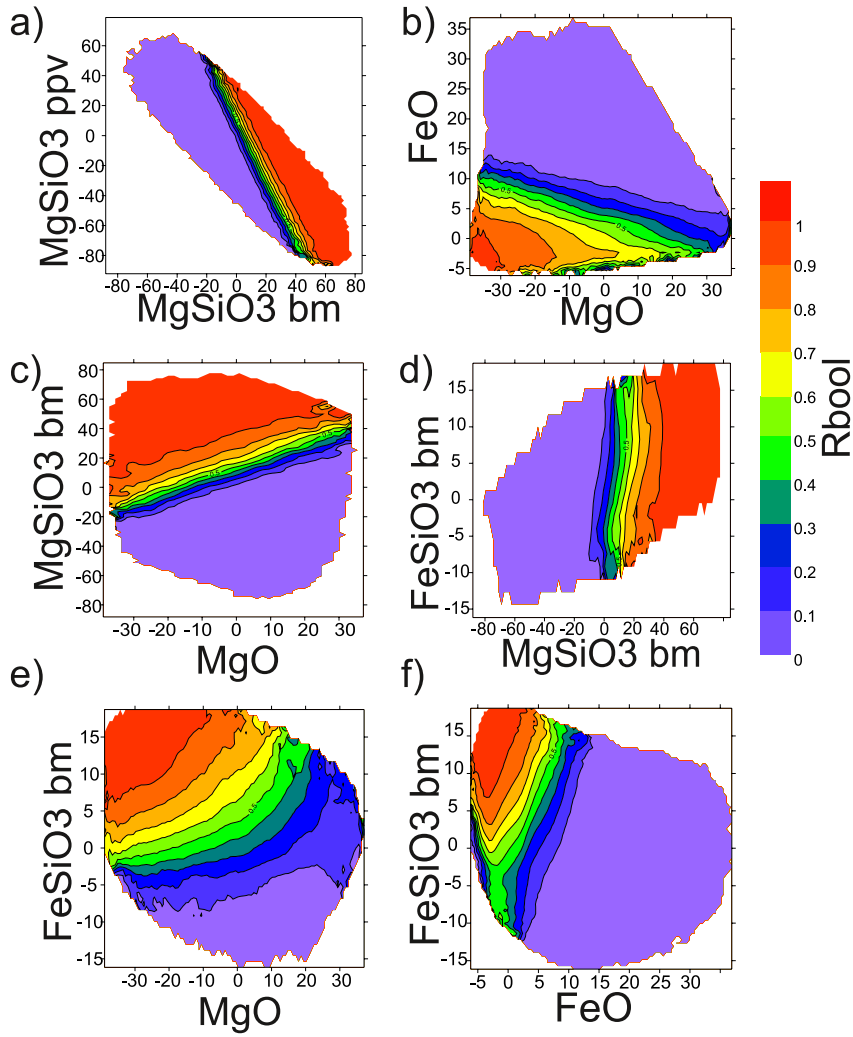

Figure 7. Same as Figure 6, but for the case that both *Vp* and *Vs* decrease across the D" reflector.

purple regions in other plots) $R < 3$ is predominantly produced, whereas Rbool values close to unity (white regions in Figures 6a and 6b, orange regions in the other plots) indicate $R \geq 3$ is dominant.

The Rbool data sets form the basis for the figures in the following section and the Supporting Information (Figures 6 and 7, Figures S5–S7 in Supporting Information S1). To determine which parameters are most relevant for generating large *R*-values, we also look at the boundary between high and low *R*-values. If a boundary is vertical, as shown in Figure 6b, mineral C is important for generating large *R*-values while mineral D is not important (likewise for horizontal boundaries, but then mineral C is not important while mineral D is). If the boundary is slanted (Figure 6a) both minerals have to change for generating large *R*-values. The aim is to thereby identify (a) which parameters are most and least relevant for producing $R \geq 3$, (b) which combinations of parameter ranges are necessary and sufficient for this, and (c) to what extent transitions between low and high-*R* regimes are sharp boundaries (steep gradients).

5. Large *R*-Values

First, we look at the case of both *P* and *S* velocities increasing across the discontinuity for the mantle model (d*Vp* and d*Vs* > 0): our analysis shows that a change from $MgSiO_3$-bridgmanite (bm) to $MgSiO_3$-post-perovskite (ppv) is most important for the generation of *R*-values ≥ 3 (orange-red colors in Figure 6). Figure 6c shows that a decrease of bm is balanced with an increase in ppv for large *R*-values; however, when comparing the change of

$MgSiO_3$ bm to $FeSiO_3$ bm across the boundary, we find that the reduction of $MgSiO_3$ bm is the important parameter, since the dividing line between high and low *R*-values is almost vertical in Figure 6f. The same is true for $MgSiO_3$-ppv and $FeSiO_3$-ppv in that the $MgSiO_3$-ppv increase is more important that the $FeSiO_3$ increase (Figure S5e in Supporting Information S1).

We find that a large increase of MgO across the boundary and a moderate increase of FeO across the boundary can generate large *R*-values (Figure 6d). But if an increase of FeO is found, then a small increase of Mg-ppv is sufficient for producing large *R*-values (Figure 6e). Since we find that an increase of MgO can generate *R*-values ≥ 3, we map MgO, $MgSiO_3$-ppv and $MgSiO_3$-bm and find that the region of high (≥ 3) and low *R*-values is separated by a steep and narrow boundary (Figure S6 in Supporting Information S1). The figure shows that high *R*-values are possible for an increase in ppv while bm is decreasing (i.e., a phase transformation) if at the same time MgO is also increasing.

Looking at other parameters (Figure S5 in Supporting Information S1), we find that varying temperature does not cause large *R*-values, since temperature changes seem to induce changes in *Vp* and *Vs* that are comparable in size. Indeed, Deschamps and Trampert (2003) show that temperature variations can lead to an *R*-value of 1.5–2. In our models, the partitioning of iron between bm and ferropericlase also seems to have little influence. Andrault et al. (2010) showed that Fe partitions preferably into bm and leaves post-perovskite Fe-poor. However, we only looked at partitioning between [Mg, Fe]SiO_3 and [Mg, Fe]O in our models, and therefore the case described by Andrault et al. (2010) is not represented in our models. Lastly, we find that an increase or decrease of pure SiO_2 phase (seifertite), or Al in bridgmanite and/or post-perovskite, do not produce large *R*-values either.

The above-mentioned results were for cases with d*Vp* and d*Vs* > 0. Contrastingly, for d*Vp* and d*Vs* < 0 across the boundary, we find the opposite behavior: a reduction of FeO and MgO or a decrease of post-perovskite (either $FeSiO_3$-ppv or $MgSiO_3$-ppv) while increasing bm is needed to have large *R*-values (Figures 7a and 7b). However, a reduction of ppv across the boundary is unrealistic, since post-perovskite is inferred to be at a depth corresponding to the D" region rather than above it (e.g., Grocholski et al., 2012). This suggests that the most relevant explanation for generating large *R*-values in regions where the *P* and *S* velocity are both decreasing is an increase of bm and a reduction of MgO and FeO, with the effect of reducing MgO being stronger than that of reducing FeO.

The data set of mantle models containing a MORB component (Table S3 and Figure S7 in Supporting Information S1) shows similar results: For cases where *Vp* and *Vs* both increase across the D" reflector, an increase of ppv and a decrease of bm is the important scenario for producing large *R*-values. In the case of both velocities decreasing, a reduction of MgO and FeO or a decrease of the amount of ppv with increase of bm across the reflector would generate *R*-values of 3 and higher. Note that the amount of FeO and MgO come from the non-MORB component in the bulk assemblage, since MORB does not contain MgO or FeO.

6. Discussion

The exact mineralogy of the lowermost mantle is still being debated (e.g., Cobden et al., 2009; Davies et al., 2015; Houser et al., 2020; Trønnes, 2010; Vilella et al., 2021) and seismological mapping of structures near the CMB has helped to test several possibilities of mantle mineralogy. While the mineral phase transition from bridgmanite to post-perovskite seems to be a good explanation for regions of past subduction (e.g., Hernlund et al., 2005; Trønnes, 2010), the mineralogy in the LLSVPs where slower-than-average velocities exist is still not well understood (e.g., Deschamps et al., 2012, 2015; Koelemeijer, 2021; McNamara, 2019). In several cases, waves reflecting from layers inside these large low-velocity structures have been used to determine the velocity change across the reflectors (e.g., Lay et al., 2006; Schumacher et al., 2018), which provides a constraint on mineralogy (e.g., Ohta et al., 2008). We use our thermochemical modeling results in combination with PdP and SdS polarity information to constrain mineralogy and causes for the D" reflector.

When interpreting polarity variations in *P* and *S* waves while ignoring those cases where changes in *P* wave and *S* wave velocity have opposite signs, there are essentially four possible cases (Figure 8 and Table 2). These four cases separate into two groups where *Vp* and *Vs* both increase (Case 1), and two groups where *Vp* and *Vs* decrease (Case 2), with either the same or opposite polarity of PdP- and SdS-waves.

If *Vp* and *Vs* both increase, and the ratio (*R*) between *S* wave velocity change and *P* wave velocity change is between 1 and 3 (Figure 8, case 1a), D" reflection polarities for *P* and *S* waves are the same as the main phase

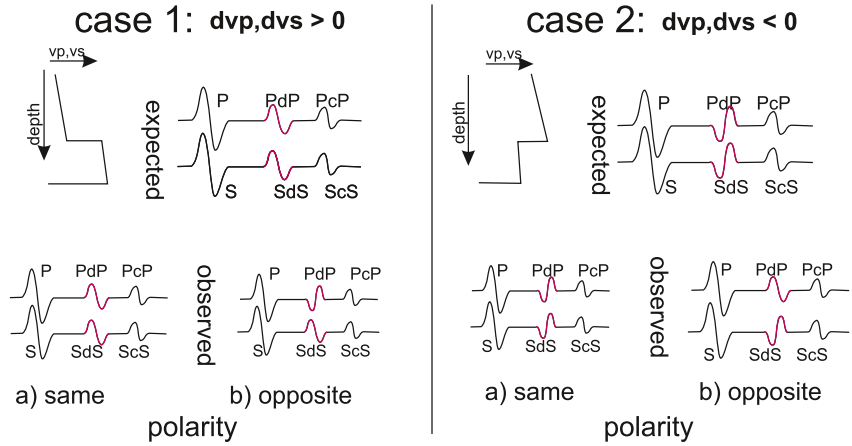

Figure 8. Overview of the different cases: left hand side: *Vp* and *Vs* both increasing across the reflector, Case 1, with expected waveforms, right hand side: *Vp* and *Vs* both decreasing across the reflector, Case 2, with expected waveforms. The possibilities of observed polarities of PdP (SdS) as (a) same and (b) opposite to *P*(*S*) and PcP(ScS) are shown in the bottom row, referring to Cases 1a and 1b and Cases 2a and 2b, respectively, in Table 2.

(*P* or *S*) and the CMB reflection. This case has been observed in several seismic data sets using *P* and *S* waves together (e.g., Cobden & Thomas, 2013; Pisconti et al., 2019; C. Thomas & Weber, 1997; Weber, 1993). Such a scenario could be produced by a thermal anomaly (e.g., Lay et al., 2004; C. Thomas, Kendall, & Lowman, 2004), or alternatively, by subducted mid-ocean ridge basalt, MORB (Cobden & Thomas, 2013; Deschamps et al., 2012; Hirose et al., 1999; Vilella et al., 2021), which is silica-saturated and does not contain ferropericlase. Our modeling shows that an *R*-value between 1 and 3 can be generated by an increase of bm or a decrease of FeO and MgO (Figure 6, purple colors), and this reduction in bulk (Mg, Fe)O can be indicative of the presence of MORB. Our analyses of mantle models containing a MORB component support this assumption and we therefore conclude that the event shown in Figure 4c is most likely reflections off MORB residing in the D" region, since *S* wave observations in this region also show polarities consistent with a velocity increase (Kendall & Nangini, 1996; Lay et al., 2004). For the two events in Figures 4a and 4b, no clear explanation is possible, since we are missing *S* wave polarity information for this region.

If, for an *S* velocity increase across D", the PdP polarity would indicate a velocity decrease, there are two explanations: Either there is indeed a *P* velocity decrease with an associated *S* wave velocity increase across the D" reflector, as indicated by for example, Wookey et al. (2005) for the ppv phase transition in pure $MgSiO_3$. Alternatively, an *R*-value larger than 3 could generate the same effect (case 1b in Table 2 and Figure 8). Our thermochemical modeling shows that the ppv phase transition is again a good explanation for this scenario (Figure 6, Table 2). Indeed, the contrast of the *P* wave velocity across the post-perovskite phase transition has been reported to be

Table 2
The Four Cases Shown in Figure 8 With Their Previous Interpretation

	Case 1a	Case 1b	Case 2a	Case 2b
Polarities, PdP vs. SdS	Same	Opposite	Same	Opposite
Previous interpretation	MORB, cold slab	ppv (in $MgSiO_3$)	ppv in MORB, seifertite trans.	
R-value range	$1 < R < 3$	$R \geq 3$	$1 < R < 3$	$R \geq 3$
Mineralogy change across D"	+bm, –ppv	-bm, +ppv	+ppv, -bm	+bm, –ppv
	–MgO, –FeO	+MgO, +FeO	+FeO	–MgO, (–FeO)
Interpretation with *R*-value	Consistent with MORB	Consistent with ppv phase trans.	Consistent with ppv phase trans in MORB	Primordial material, BEAMs

Note. In the third row, we provide the *R*-value associated with the polarities PdP vs. SdS in the first row and the fourth row explains the mineralogy changes that cause the *R*-values in row 3. The last row gives our interpretation for each case.

between ±1%, while the *S* wave change is between 1% and 4% (Oganov & Ono, 2004; Tsuchiya & Tsuchiya, 2006; for an overview see e.g., Cobden et al., 2015).

There is potentially another mechanism that could generate the polarities shown in case 1b: an increase of MgO and FeO across the boundary would also generate large *R*-values. While the decomposition of (Mg, Fe)-bm into (Mg, Fe)O and SiO_2 has been suggested in early experimental studies (e.g., Dobrovinsky et al., 1998; Saxena et al., 1996), more recent studies indicate that the decomposition could have arisen through a problem with the experimental setup (Gong et al., 2004; Mao et al., 1997). Hence, we suggest that the post-perovskite phase transition is the best explanation for observations of PdP polarities opposite those of *P* and PcP together with SdS polarities the same as *S* and ScS (case 1b).

The mineralogy in low-velocity regions, especially in the LLSVP beneath Africa and the Pacific, is less well constrained, and different mechanisms for velocity discontinuities within LLSVPs have been discussed. Ohta et al. (2008) show that the post-perovskite phase transition in MORB could generate a reflector, but the stishovite to seifertite transition could also be a candidate for this observation (Andrault et al., 2014; Tsuchiya et al., 2004), although the depth of the transition is still debated (Grocholski et al., 2013; Ohta et al., 2008; Sun et al., 2019). Both cases would show polarities of PdP and SdS consistent with a velocity decrease as represented by case 2a in Table 2. Our modeling shows that an *R*-value below 3 is consistent with the ppv phase transition within MORB while bm decreases.

A velocity decrease for both, *P* and *S* waves with a ratio of d*Vs*/d*Vp* of ∼3 is, on the other hand, indicative of melt in the lower mantle (e.g., Berryman, 2000; Hier-Majumder, 2008), but melt has previously been discussed as cause for ultralow velocity zones (e.g., Rost et al., 2006, 2005; Yu & Garnero, 2018) rather than for a 300 km thick D" layer, and it is still discussed whether melt would stay at the CMB (Garnero, 2000; C. W. Thomas et al., 2012). It is difficult to envisage a dynamic mechanism in which thin melt layers would pond 300 km above the CMB, although seismically it would not be incompatible with our observations. A 300 km thick layer of (partial) melt is incompatible with observations of the *P* and *S* wave speed structure within D" (e.g., Cobden et al., 2012).

Lastly, case 2b, where a velocity decrease across the D" reflector is expected in *S* waves, but where the PdP polarity suggests a velocity increase (Figure 8, Case 2b), is possibly the rarest observation up to now. We find such a case in the region beneath the western Pacific (Figure 5, see also C. Thomas & Laske, 2015) with PdP waves showing a polarity that is the same as *P* and PcP in a part of the Pacific LLSVP (Figure 5). Near this region, the *S* wave study of Konishi et al. (2009), on the other hand, found a velocity decrease at the top of D" (interpreted there as a phase transition within MORB). While not exactly in the same region, the results by Konishi et al. (2009) together with our results would suggest that our observed *P* wave polarity is due to large *R*-values, and hence would confirm that *S* wave velocity reductions are at least 3 times as strong as *P* wave velocity reductions in this part of the LLSVP, as also indicated by Koelemeijer et al. (2016, 2018). The reduction of *S* wave velocity suggests that MORB itself is not a good explanation for this region (Deschamps et al., 2012), and the *P* wave polarity results (Figure 5) indicate that the ppv phase transition is not satisfactory either. Instead, our thermochemical modeling shows that an increase in bm or a decrease in MgO (and to a smaller degree FeO) would generate large *R*-values.

Ballmer et al. (2016) model the Pacific LLSVP with a combination of MORB and primordial material, which generates a velocity discontinuity at depths consistent with the D" reflector within an LLSVP-like region (Schumacher et al., 2018). Furthermore, Deschamps et al. (2012) and Vilella et al. (2021) show that an increase of bm with an increase of Fe has been suggested to be responsible for the LLSVPs. Their composition is similar to BEAMs (bridgmanite enriched ancient material, Ballmer et al., 2017) and if the BEAMs exist near the CMB (Gülcher et al., 2020) this could explain case 2b in Table 2. Our thermochemical modeling suggests that an increase in bm has the largest effect, but it may also be accompanied with a decrease of FeO (Figure 7f). Interestingly, the studies by Chandler et al. (2021), although aimed at constraining anisotropy near the edges of an LLSVP, also find that outside the LLSVP ppv is a good explanation, while inside the LLSVP bm explains their observations better.

Our modeling has shown that the different polarity information of *P* and *S* waves, when jointly considered, can aid to constrain the mineralogy of the D" region in different settings. While we are focusing here on isotropic minerals and combinations of minerals above and below the D" reflector to explain polarities, we have to keep

in mind that anisotropy is another mechanism that causes polarity changes in seismic waves. For example, C. Thomas et al. (2011), Pisconti et al. (2019), and Creasy et al. (2021, 2019) show that polarity variations, especially of *P* waves reflected at the D" layer, can also be generated by anisotropy of the D" minerals (ppv, bm, and even ferropericlase), even over small azimuth ranges. The anisotropy, generated by the flow of anisotropic minerals in D", will, however, cause polarity observations that vary with azimuth as shown in Pisconti et al. (2019); these are unlike the results here, where polarity variations are isotropic. In addition, when anisotropy is present in the D" region, ScS-waves will experience directionally dependent splitting (Nowacki et al., 2011). It has been shown that a combination of splitting measurements together with PdP and SdS polarity observations (Pisconti et al., 2019), and including discrepant SKS and SKKS splitting measurements (e.g., Creasy et al., 2021) can further constrain mineralogy in the D" region, but the observations vary with azimuth due to the directional velocity variations of the deformed minerals. Therefore, a mapping of regions such as beneath the Caribbean or the western Pacific with crossing paths and taking shear wave splitting of ScS waves into account would help to discriminate between the alternative hypotheses of anisotropy vs. large *R*-values.

7. Conclusion

We have shown that distance-dependent polarity observations of *P* wave reflections depend on the ratio of change of *S* wave velocity with respect to change in *P* wave velocity across the D" reflector, referred to here as the *R*-value. LDA of mineral composition paired with a set of velocities derived from thermochemical modeling enables us to generate a profile of distinct observable classes (namely, *R*-values smaller or larger than 3 for regions with velocity increases or decreases), allowing the seismological observables to inform the characterization of regions in terms of typical mineralogical constituent ratios.

The statistically significant results derived from the thermo-chemical modeling data suggest different causes for large *R*-values. The post-perovskite phase transition is the best explanation for regions where a velocity increase is detected with *S* waves while the *P* wave has a polarity that would indicate an apparent velocity decrease. In regions where both D"-reflected *P* and *S* waves have polarities opposite to the main phases, the ppv phase transition within MORB is likewise the best explanation, as already reported in previous work. A reflection at a MORB layer is consistent with *P* and *S* wave polarities both suggesting a velocity increase. The last case of an SdS-wave with a polarity opposite to *S* and ScS but with a PdP-wave suggesting a positive velocity jump across D", as seen in one region of the Pacific LLSVP, can be explained by a reflection off bridgmanite-enriched material, thereby further constraining mineralogy in the LLSVP regions.

Analyzing polarities of *P* and *S* waves, together with extending the epicentral distance range to lower values than previously, and for different regions, thus allows a better classification of the mineralogy change across a reflector. Since variable polarities of *P* waves and *S* waves can also be generated by anisotropy in the D" region, as shown by Pisconti et al. (2019) and C. Thomas et al. (2011), a detailed analysis of *P* and *S* wave observations covering a variety of distances and azimuths is necessary to discriminate between these two hypotheses of large *R*-values vs. anisotropy. Where the former is supported and the latter is absent, inferences can be drawn regarding the most likely mineralogical constituent ratios across the reflector.

Data Availability Statement

All data used here are freely accessible through IRIS (Incorporated Research Institutions for Seismology). The dois and references for the data sets are given in Table S2 in Supporting Information S1, the events parameters are shown in Table S1 in Supporting Information S1. The authors use data from Tibet (Geodynamics of Indentor Corners (Namche Barwa Tibet), https://doi.org/10.7914/SN/XE_2003, Meltzer (2003)), the Transportable Array, https://doi.org/10.7914/SN/TA, IRIS Transportable Array (2003), and the PLUME data (Plume-Lithosphere Undersea Melt Experiment Phase 1 and 2 and permanent stations, FDSN code YS, Laske et al., 2009).

Acknowledgments
The authors would like to thank the Editor, Carolina Lithgow-Bertelloni, and two anonymous reviewers for their constructive comments that improved this manuscript. Part of this study was financed by the bilateral Deutsche Forschungsgemeinschaft and Agence Nationale de la Recherche (DFG-ANR) TIMEleSS project (ANR-17-CE31-0025; TH 1530/18-1; SA 2585/3-1; SP1216/8-1), the bilateral PROCOPE-PPP program (PHC 40555PC; DAAD 57390184) and a Vidi grant from the Dutch Research Council (NWO), number 016.Vidi.171.022 (LC). The authors would like to thank Jennifer Jackson and Carmen Sanchez-Valle for discussions on large *R*-values and mineralogy in D". Seismic data were analyzed with Seismic Handler (Stammler, 1993) and maps were drawn with GMT (Wessel & Smith, 1995). Statistics were performed using the Eigen C++ template library for linear algebra (https://eigen.tuxfamily.org).

References

Aki, K., & Richards, P. (1980). Quantitative seismology (Vol. *I*, sec. 5.2).

Andrault, D., Muñoz, M., Bolfan-Casanova, N., Guignot, N., Perrillat, J. P., Aquilanti, G., & Pascarelli, S. (2010). Experimental evidence for perovskite and post-perovskite coexistence throughout the whole D" region. *Earth and Planetary Science Letters*, *293*, 90–96. https://doi.org/10.1016/j.epsl.2010.02.026

Andrault, D., Trønnes, R. G., Konôpková, Z., Morgenroth, W., Liermann, H. P., Morard, G., & Mezouar, M. (2014). Phase diagram and *P-V-T* equation of state of Al-bearing seifertite at lowermost mantle conditions. *American Mineralogist*, *99*, 2035–2042. https://doi.org/10.2138/am-2014-4697

Ballmer, M. D., Houser, C., Hernlund, J. W., Wentzcovitch, R. M., & Hirose, K. (2017). Persistence of strong silica-enriched domains in the Earth's lower mantle. *Nature Geoscience*, *10*, 236–240. https://doi.org/10.1038/ngeo2898

Ballmer, M. D., Schumacher, L., Lekic, V., Thomas, C., & Ito, G. (2016). Compositional layering within the large low shear-wave velocity provinces in the lower mantle. *Geochemistry, Geophysics, Geosystems*, *17*, 5056–5077. https://doi.org/10.1002/2016GC006605

Berryman, J. G. (2000). Seismic velocity decrement ratios for regions of partial melt in the lower mantle. *Geophysical Research Letters*, *27*, 421–424. https://doi.org/10.1029/1999gl008402

Bortfeld, R. (1961). Approximations to the reflection and transmission coefficients of plane longitudinal and transverse waves. *Geophysical Prospecting*, *9*, 485–502. https://doi.org/10.1111/j.1365-2478.1961.tb01670.x

Bréger, L., & Romanowicz, B. (1998). Three-dimensional structure at the base of the mantle beneath the central Pacific. *Science*, *282*, 718–720.

Bullen, K. E. (1949). Compressibility-pressure hypothesis and the Earth's interior. *Monthly Notices of the Royal Astronomical Society*, *5*(1949), 355–368. https://doi.org/10.1111/j.1365-246x.1949.tb02952.x

Catalli, K., Shim, S. H., & Prakapenka, V. (2009). Thickness and Clapeyron slope of the post-perovskite boundary. *Nature*, *462*, 782–785. https://doi.org/10.1038/nature08598

Červený, V. (2001). *Seismic ray theory*. Cambridge University Press.

Chaloner, J. W., Thomas, C., & Rietbrock, A. (2009). *P* and *S* wave reflectors in D" beneath southeast Asia. *Geophysical Journal International*, *179*, 1080–1092. https://doi.org/10.1111/j.1365-246X.2009.04328.x

Chandler, B. C., Chen, L.-W., Li, M., Romanowicz, B., & Wenk, H.-R. (2021). Seismic anisotropy, dominant slip systems, and phase transitions in the lowermost mantle. *Geophysical Journal International*, *227*, 1665–1681. https://doi.org/10.1093/gji/ggab278

Cobden, L., Goes, S., Ravenna, M., Styles, E., Cammarano, F., Gallagher, K., & Connolly, J. A. D. (2009). Thermochemical interpretation of 1-D seismic data for the lower mantle: The significance of nonadiabatic thermal gradients and compositional heterogeneity. *Journal of Geophysical Research*, *114*, B11309. https://doi.org/10.1029/2008JB006262

Cobden, L., Mosca, I., Trampert, J., & Ritsema, J. (2012). On the likelihood of post-perovskite near the core-mantle boundary: A statistical interpretation of seismic observations. *Physics of the Earth and Planetary Interiors*, *210*, 21–35. https://doi.org/10.1016/j.pepi.2012.08.007

Cobden, L., & Thomas, C. (2013). The origin of D" reflections: A systematic study of seismic array data sets. *Geophysical Journal International*, *194*, 1091–1118.

Cobden, L., Thomas, C., & Trampert, J. (2015). Seismic detection of post-perovskite inside the Earth. In *Earth's heterogeneous mantle* (pp. 391–440). Springer. https://doi.org/10.1007/978-3-319-15627-9_13

Cormier, V. F. (1982). The effect of attenuation on seismic body waves. *Bulletin of the Seismological Society of America*, *72*, S169–S200.

Creasy, N., Pisconti, A., Long, M., & Thomas, C. (2021). Modeling of seismic anisotropy observations reveals plausible lowermost mantle flow directions beneath Siberia. *Geochemistry, Geophysics, Geosystems*, *22*, e2021GC009924. https://doi.org/10.1029/2021GC009924

Creasy, N., Pisconti, A., Long, M. D., Thomas, C., & Wookey, J. (2019). Constraining lowermost mantle anisotropy with body waves: A synthetic modeling study. *Geophysical Journal International*, *217*, 766–783. https://doi.org/10.1093/gji/ggz049

Crewes Explorer Programs. (2022). Crewes Explorer Programs. Retrieved from https://www.crewes.org/ResearchLinks/ExplorerPrograms

Davies, D. R., Goes, S., & Lau, H. C. P. (2015). Thermally dominated deep mantle LLSVP, a review. In *Earth's heterogeneous mantle*. Springer. https://doi.org/10.1007/978-3-319-15627-9

Davies, D. R., Kelly, E. J., & Filson, J. R. (1971). Vespa process for analysis of seismic signals. *Nature Physical Science*, *232*, 8–13. https://doi.org/10.1038/physci232008a0

Deschamps, F., Cobden, L., & Tackley, P. J. (2012). The primitive nature of large low shear-wave velocity provinces. *Earth and Planetary Science Letters*, *349–350*, 198–208. https://doi.org/10.1016/j.epsl.2012.07.012

Deschamps, F., Li, Y., & Tackley, P. J. (2015). Large-scale thermo-chemical structure of the deep mantle: Observations and models. In *Earth's heterogeneous mantle*. Springer. https://doi.org/10.1007/978-3-319-15627-9

Deschamps, F., & Trampert, J. (2003). Mantle tomography and its relation to temperature and composition. *Physics of the Earth and Planetary Interiors*, *140*, 277–291. https://doi.org/10.1016/j.pepi.2003.09.004

Dobrosavljevic, V. V., Sturhahn, W., & Jackson, J. M. (2019). Evaluating the role of iron-rich (Mg, Fe)O in ultralow velocity zones. *Minerals*, *9*, 1–16. https://doi.org/10.3390/min9120762

Dubrovinsky, L., Saxena, S. K., Ahuja, R., & Johansson, B. (1998). Theoretical study of the stability of $MgSiO_3$-perovskite in the deep mantle. *Geophysical Research Letters*, *25*, 4253–4256. https://doi.org/10.1029/1998gl900141

Duda, R. O., & Hart, P. E. (1973). *Pattern classification and scene analysis*. John Wiley & Sons.

Fisher, R. A. (1936). The use of multiple measurements in taxonomic problems. *Annual Eugenics*, *7*, 179–188. https://doi.org/10.1111/j.1469-1809.1936.tb02137.x

Frederiksen, A. (2022). Javascript solver for the Zoeppritz equations. Retrieved from https://home.cc.umanitoba.ca/~frederik/Software/Zoeppritz

Garnero, E. J. (2000). Heterogeneity of the lowermost mantle. *Annual Review of Earth and Planetary Sciences*, *28*, 509–537. https://doi.org/10.1146/annurev.earth.28.1.509

Gong, Z., Fei, Y., Dai, F., Zhang, L., & Jing, F. (2004). Equation of state and phase stability of mantle perovskite up to 140 GPa shock pressure and its geophysical implications. *Geophysical Research Letters*, *31*. L04614. https://doi.org/10.1029/2003gl019132

Grocholski, B., Catalli, K., Shim, S. H., & Prakapenka, V. (2012). Mineralogical effects on the detectability of the postperovskite boundary. *Proceedings of the National Academy of Sciences of the United States of America*, *109*, 2275–2279. https://doi.org/10.1073/pnas.1109204109

Grocholski, B., Shim, S.-H., & Prakapenka, V. B. (2013). Stability, metastability, and elastic properties of a dense silica polymorph, seifertite. *Journal of Geophysical Research*, *118*, 4745–4757. https://doi.org/10.1002/jgrb.50360

Gülcher, A. J. P., Gebhardt, D. J., Ballmer, M. D., & Tackley, P. J. (2020). Variable dynamic styles of primordial heterogeneity preservation in the Earth's lower mantle. *Earth and Planetary Science Letters*, *536*, 116160. https://doi.org/10.1016/j.epsl.2020.116160

Hernlund, J. W. (2010). On the interaction of the geotherm with a post-perovskite phase transition in the deep mantle. *Physics of the Earth and Planetary Interiors*, *180*, 222–234. https://doi.org/10.1016/j.pepi.2010.02.001

Hernlund, J. W., & Houser, C. (2008). On the statistical distribution of seismic velocities in Earth's deep mantle. *Earth and Planetary Science Letters*, *265*, 423–437. https://doi.org/10.1016/j.epsl.2007.10.042

Hernlund, J. W., Thomas, C., & Tackley, P. J. (2005). A doubling of the post-perovskite phase boundary and structure of the Earth's lowermost mantle. *Nature*, *434*, 882–886. https://doi.org/10.1038/nature03472

Hier-Majumder, S. (2008). Influence of contiguity on seismic velocities of partially molten aggregates. *Journal of Geophysical Research*, *113*, 1–14. https://doi.org/10.1029/2008JB005662

Hirose, K., Fei, Y., Ma, Y., & Mao, H. K. (1999). The fate of subducted basaltic crust in the Earth's lower mantle. *Nature*, *397*, 53–56. https://doi.org/10.1038/16225

Hosseini, K., Matthews, K. J., Sigloch, K., Shephard, G. E., Domeier, M., & Tsekhmistrenko, M. (2018). SubMachine: Web-Based tools for exploring seismic tomography and other models of Earth's deep interior. *Geochemistry, Geophysics, Geosystems*, *19*. https://doi.org/10.1029/2018GC007431

Hosseini, K., Sigloch, K., Tsekhmistrenko, M., Zaheri, A., Nissen-Meyer, T., & Igel, H. (2020). Global mantle structure from multifrequency tomography using *P*, PP, and *P*-diffracted waves. *Geophysical Journal International*, *220*, 96–141. https://doi.org/10.1093/gji/ggz394

Houser, C., Hernlund, J. W., Valencia-Cardona, J., & Wentzcovitch, R. M. (2020). Discriminating lower mantle composition. *Physics of the Earth and Planetary Interiors*, *308*, 106552. https://doi.org/10.1016/j.pepi.2020.106552

Hutko, A. R., Lay, T., Revenaugh, J., & Garnero, E. J. (2008). Anticorrelated seismic velocity anomalies from post-perovskite in the lowermost mantle. *Science*, *320*, 1070–1074. https://doi.org/10.1126/science.1155822

IRIS Transportable Array. (2003). *U.S. Array Transportable Array*. International Federation of Digital Seismograph Networks. https://doi.org/10.7914/SN/TA

Jackson, J. M., & Thomas, C. (2021). Seismic and mineral physics constraints on the D″ layer. In H. Marquardt, M. Ballmer, S. Cottaar, & J. Konter (Eds.), *Mantle convection and surface expressions*.https://doi.org/10.1002/9781119528609.ch8

Karato, S.-I., & Karki, B. B. (2001). Origin of lateral variation of seismic wave velocity and density in the deep mantle. *Journal of Geophysical Research*, *106*, 21771–21783. https://doi.org/10.1029/2001jb000214

Kawai, K., & Geller, R. J. (2010). Waveform inversion for localized seismic structure and an application to D″ structure beneath the Pacific. *Journal of Geophysical Research*, *115*, 1–15. https://doi.org/10.1029/2009jb006503

Kendall, J.-M., & Nangini, C. (1996). Lateral variations in below the Caribbean. *Geophysical Research Letters*, *23*, 399–402. https://doi.org/10.1029/95gl02659

Kennett, B., Engdahl, E., & Buland, R. (1995). Constraints on seismic velocities in the Earth from travel times. *Geophysical Journal International*, *122*, 108–124. https://doi.org/10.1111/j.1365-246x.1995.tb03540.x

Kito, T., Rost, S., Thomas, C., & Garnero, E. J. (2007). New insights into the *P* and *S* wave velocity structure of the D″ discontinuity beneath the Cocos plate. *Geophysical Journal International*, *169*, 631–645. https://doi.org/10.1111/j.1365-246X.2007.03350.x

Koelemeijer, P. (2021). Toward consistent seismological models of the core-mantle boundary landscape. In H. Marquardt, M. Ballmer, S. Cottaar, & J. Konter (Eds.), *Mantle convection and surface expressions*. https://doi.org/10.1002/9781119528609.ch9

Koelemeijer, P., Ritsema, J., Deuss, A., & van Heijst, H. J. (2016). SP12RTS: A degree-12 model of shear- and compressional-wave velocity for Earth's mantle. *Geophysical Journal International*, *204*, 1024–1039. https://doi.org/10.1093/gji/ggv481

Koelemeijer, P., Schuberth, B. S. A., Davies, D. R., Deuss, A., & Ritsema, J. (2018). Constraints on the presence of post-perovskite in Earth's lowermost mantle from tomographic-geodynamic model comparisons. *Earth and Planetary Science Letters*, *494*, 226–238. https://doi.org/10.1016/j.epsl.2018.04.056

Konishi, K., Kawai, K., Geller, R. J., & Fuji, N. (2009). MORB in the lowermost mantle beneath the western Pacific: Evidence from waveform inversion. *Earth and Planetary Science Letters*, *278*, 219–225. https://doi.org/10.1016/j.epsl.2008.12.002

Kuwayama, Y., Hirose, K., Cobden, L., Kusakabe, M., Tateno, S., & Ohishi, Y. (2022). Post-perovskite phase transition in the pyrolitic lowermost mantle: Implications for ubiquitous occurrence of post-perovskite above CMB. *Geophysical Research Letters*, *49*, e2021GL096219. https://doi.org/10.1029/2021GL096219

Laske, G., Collins, J. A., Wolfe, C. J., Solomon, S. C., Detrick, R. S., Orcutt, J. A., et al. (2009). Probing the Hawaiian hot spot with new ocean bottom instruments. *Eos Transactions American Geophysical Union*, *90*(41), 362–363. https://doi.org/10.1029/2009EO410002

Lay, T. (2008). Sharpness of the D″ discontinuity beneath the Cocos plate: Implications for the perovskite to post-perovskite phase transition. *Geophysical Research Letters*, *35*, 1–5. https://doi.org/10.1029/2007GL032465

Lay, T. (2015). Deep Earth structure: Lower mantle and D". In *Treatise Geophysics* (2nd ed., Vol. 1). Elsevier B.V. https://doi.org/10.1016/B978-0-444-53802-4.00019-1

Lay, T., & Garnero, E. J. (2004). Core-mantle boundary structures and processes. In R. Sparks & C. Hawkesworth (Eds.), *The state of the planet: Frontiers and challenges in Geophysics*. https://doi.org/10.1029/150GM04

Lay, T., Garnero, E. J., & Russell, S. A. (2004). Lateral variation of the D″ discontinuity beneath the cocos plate. *Geophysical Research Letters*, *31*. https://doi.org/10.1029/2004GL020300

Lay, T., & Helmberger, D. V. (1981). Body wave amplitude patterns and upper mantle attenuation variations across North America. *Geophysical Journal International*, *68*, 691–726. https://doi.org/10.1111/j.1365-246x.1981.tb04895.x

Lay, T., & Helmberger, D. V. (1983). A lower mantle *S* wave triplication and the shear velocity structure of D. *Geophysical Journal of the Royal Astronomical Society*, *75*, 799–837. https://doi.org/10.1111/j.1365-246x.1983.tb05010.x

Lay, T., Hernlund, J., Garnero, E. J., & Thorne, M. S. (2006). A post-perovskite lens and D″ heat flux beneath the central Pacific. *Science*, *314*, 1272–1276.

Li, C., Van Der Hilst, R. D., Engdahl, E. R., & Burdick, S. (2008). A new global model for *P* wave speed variations in Earth's mantle. *Geochemistry, Geophysics, Geosystems*, *9*. https://doi.org/10.1029/2007GC001806

Malcolm, A. E., & Trampert, J. (2011). Tomographic errors from wavefront healing: More than just a fast bias. *Geophysical Journal International*, *185*, 385–402. https://doi.org/10.1111/j.1365-246X.2011.04945.x

Mao, H. K., Shen, G., & Hemley, R. J. (1997). Multivariable dependence of Fe-Mg partitioning in the lower mantle. *Science*, *278*, 2098. https://doi.org/10.1126/science.278.5346.2098

Martinez, A. M., & Kak, A. C. (2001). PCA vs. LDA. *IEEE Transactions on Pattern Analysis and Machine Intelligence*, *23*, 228–233. https://doi.org/10.1109/34.908974

Masters, G., Laske, G., Bolton, H., & Dziewonski, A. M. (2000). The relative behavior of shear velocity, bulk sound speed, and compressional velocity in the mantle: Implications for chemical and thermal structure. In S. Karato, A. Forte, R. Liebermann, G. Masters, & L. Stixrude (Eds.), *Earth's deep interior: mineral physics and tomography from the atomic to the global scale* (Vol. 117, pp. 63–87). AGU. https://doi.org/10.1029/GM117p0063

McLachlan, G. J. (2005). *Discriminant analysis and statistical pattern recognition* (Vol. 583). John Wiley & Sons.

McNamara, A. K. (2019). A review of large low shear velocity provinces and ultralow velocity zones. *Tectonophysics*, *760*, 199–220. https://doi.org/10.1016/j.tecto.2018.04.015

Meltzer, A. (2003). *Geodynamics of indentor corners*. International Federation of Digital Seismograph Networks. https://doi.org/10.7914/SN/XE_2003

Moore, M. M., Garnero, E. J., Lay, T., & Williams, Q. (2004). Shear wave splitting and waveform complexity for lowermost mantle structures with low-velocity lamellae and transverse isotropy. *Journal of Geophysical Research*, *109*, 1–26. https://doi.org/10.1029/2003jb002546

Muirhead, K. J., & Datt, R. (1976). The Nth root process applied to seismic array data. *Geophysical Journal of the Royal Astronomical Society*, *47*, 197–210. https://doi.org/10.1111/j.1365-246x.1976.tb01269.x

Müller, G. (1985). The reflectivity method: A tutorial. *Journal of Geophysical Research*, *58*, 153–174.

Müller, G. (2007). *Theory of elastic waves, (Scientific Technical Report STR; 07/03)*. Potsdam: Deutsches GeoForschungsZentrum GFZ (p. 228). https://doi.org/10.2312/GFZ.b103-07037

Murakami, M., Hirose, K., Kawamura, K., Sata, N., & Ohishi, Y. (2004). Post-perovskite phase transition in $MgSiO_3$. *Science*, *304*, 855–858. https://doi.org/10.1126/science.1095932

Nowacki, A., Wookey, J., & Kendall, J. M. (2011). New advances in using seismic anisotropy, mineral physics, and geodynamics to understand deformation in the lowermost mantle. *Journal of Geodynamics*, *52*, 205–228. https://doi.org/10.1016/j.jog.2011.04.003

Oganov, A. R., & Ono, S. (2004). Theoretical and experimental evidence for a post-perovskite phase of $MgSiO_3$ in Earth's D″ layer. *Nature*, *430*, 445–448. https://doi.org/10.1038/nature02701

Ohta, K., Hirose, K., Lay, T., Sata, N., & Ohishi, Y. (2008). Phase transitions in pyrolite and MORB at lowermost mantle conditions: Implications for a MORB-rich pile above the core-mantle boundary. *Earth and Planetary Science Letters*, *267*, 107–117. https://doi.org/10.1016/j.epsl.2007.11.037

Pisconti, A., Thomas, C., & Wookey, J. (2019). Discriminating between causes of D″ anisotropy using reflections and splitting measurements for a single path. *Journal of Geophysical Research: Solid Earth*, *124*, 4811–4830. https://doi.org/10.1029/2018JB016993

Ritsema, J., Deuss, A., Heijst, H. J. V., & Woodhouse, J. H. (2011). S40RTS: A degree-40 shear-velocity model for the mantle from new Rayleigh wave dispersion, teleseismic traveltime, and normal-mode splitting function measurements. *Geophysical Journal International*, *184*, 1223–1236. https://doi.org/10.1111/j.1365-246X.2010.04884.x

Rochira, F., Schumacher, L., & Thomas, C. (2022). Mapping the edge of subducted slabs in the lower mantle beneath southern Asia. *Geophysical Journal International*, *230*, 1239–1252. https://doi.org/10.1093/gji/ggac110

Romanowicz, B., & Wenk, H. R. (2017). Anisotropy in the deep Earth. *Physics of the Earth and Planetary Interiors*, *269*, 58–90. https://doi.org/10.1016/j.pepi.2017.05.005

Rost, S., Garnero, E. J., & Williams, Q. (2006). Fine-scale ultralow-velocity zone structure from high-frequency seismic array data. *Journal of Geophysical Research*, *111*, B09310. https://doi.org/10.1029/2005JB004088

Rost, S., Garnero, E. J., Williams, Q., & Manga, M. (2005). Seismological constraints on a possible plume root at the core-mantle boundary. *Nature*, *435*, 666–669. https://doi.org/10.1038/nature03620

Rost, S., & Thomas, C. (2002). Array seismology: Methods and applications. *Reviews of Geophysics*, *40*. https://doi.org/10.1029/2000RG000100

Saxena, S. K., Dubrovinsky, L. S., Lazor, P., Cerenius, Y., Haggkvist, P., Hanfland, M., & Hu, J. (1996). Stability of perovskite ($MgSiO_3$) in the Earth's mantle. *Science*, *274*, 1357–1359. https://doi.org/10.1126/science.274.5291.1357

Scherbaum, F., Krüger, F., & Weber, M. (1997). Double beam imaging: Mapping lower mantle heterogeneities using combinations of source and receiver arrays. *Journal of Geophysical Research*, *102*, 507–522. https://doi.org/10.1029/96jb03115

Schimmel, M., & Paulssen, H. (1996). Steeply reflected ScSH precursors from the D" region. *Journal of Geophysical Research*, *101*, 16077–16087. https://doi.org/10.1029/96jb00934

Schumacher, L., & Thomas, C. (2016). Detecting lower mantle slabs beneath Asia and the Aleutians. *Geophysical Journal International*, *205*, 1512–1524. https://doi.org/10.1093/gji/ggw098

Schumacher, L., Thomas, C., & Abreu, R. (2018). Out-of-plane seismic reflections beneath the Pacific and their geophysical implications. *Journal of Geophysical Research: Solid Earth*, *123*, 2286–2302. https://doi.org/10.1002/2017JB014728

Schweitzer, J., Fyen, J., Mykkeltveit, S., & Kvaerna, T. (2002). Seismic arrays. In *New manual of seismological observatory practice-NMSOP* (pp. 481–532). IASPEI.

Shim, S. H. (2008). The postperovskite transition. *Annual Review of Earth and Planetary Sciences*, *36*, 569–599. https://doi.org/10.1146/annurev.earth.36.031207.124309

Shim, S. H., Duffy, T. S., Jeanloz, R., & Shen, G. (2004). Stability and crystal structure of $MgSiO_3$ perovskite to the core-mantle boundary. *Geophysical Research Letters*, *31*, L10603. https://doi.org/10.1029/2004gl019639

Simmons, N. A., Forte, A. M., Boschi, L., & Grand, S. P. (2010). GyPSuM: A joint tomographic model of mantle density and seismic wave speeds. *Journal of Geophysical Research*, *115*, 1–24. https://doi.org/10.1029/2010JB007631

Sollberger, D., Greenhalgh, S. A., Schmelzbach, C., Renterghem, C. V., & Robertsson, J. O. A. (2018). 6-C polarization analysis using point measurements of translational and rotational ground-motion: Theory and applications. *Geophysical Journal International*, *213*, 77–97. https://doi.org/10.1093/gji/ggx542

Stammler, K. (1993). Seismichandler programmable multichannel data handler for interactive and automatic processing of seismological analyses. *Computers & Geosciences*, *19*, 135–140. https://doi.org/10.1016/0098-3004(93)90110-q

Stixrude, L., & Lithgow-Bertelloni, C. (2005). Thermodynamics of mantle minerals—I. Physical properties. *Geophysical Journal International*, *162*, 610–632. https://doi.org/10.1111/j.1365-246x.2005.02642.x

Stixrude, L., & Lithgow-Bertelloni, C. (2011). Thermodynamics of mantle minerals—II. Phase equilibria. *Geophysical Journal International*, *184*, 1180–1213. https://doi.org/10.1111/j.1365-246X.2010.04890.x

Sun, N., Shi, W., Mao, Z., Zhou, C., & Prakapenka, V. B. (2019). High pressure-temperature study on the thermal equations of state of seifertite and $CaCl_2$-type SiO_2. *Journal of Geophysical Research: Solid Earth*, *124*, 12620–12630. https://doi.org/10.1029/2019JB017853

Tatham, R. H., & Krail, P. M. (2012). *Zero crossings, the elastic Brewster's angle, and physical insight into shear-wave reflections* (pp. 1–5). SEG Technical Program Expanded Abstracts. https://doi.org/10.1190/segam2012-1286.1

Thomas, C., Garnero, E. J., & Lay, T. (2004). High-resolution imaging of lowermost mantle structure under the Cocos plate. *Journal of Geophysical Research*, *109*, 834–835. https://doi.org/10.1029/2004JB003013

Thomas, C., Kendall, J. M., & Lowman, J. (2004). Lower-mantle seismic discontinuities and the thermal morphology of subducted slabs. *Earth and Planetary Science Letters*, *225*, 105–113. https://doi.org/10.1016/j.epsl.2004.05.038

Thomas, C., & Laske, G. (2015). D″ observations in the Pacific from PLUME Ocean bottom seismometer recordings. *Geophysical Journal International*, *200*, 851–862. https://doi.org/10.1093/gji/ggu441

Thomas, C., & Weber, M. (1997). *P* velocity heterogeneities in the lower mantle determined with the German Regional Seismic Network: Improvement of previous models and results of 2D modeling. *Physics of the Earth and Planetary Interiors*, *101*, 105–117. https://doi.org/10.1016/S0031-9201(96)03245-1

Thomas, C., Weber, M., Agnon, A., & Hofstetter, A. (1998). A low-velocity lamella in D". *Geophysical Research Letters*, *25*, 2885–2888. https://doi.org/10.1029/98gl52103

Thomas, C., Wookey, J., Brodholt, J., & Fieseler, T. (2011). Anisotropy as cause for polarity reversals of D″ reflections. *Earth and Planetary Science Letters*, *307*, 369–376. https://doi.org/10.1016/j.epsl.2011.05.011

Thomas, C. W., Liu, Q., Agee, C. B., Asimow, P. D., & Lange, R. A. (2012). Multi-technique equation of state for Fe_2SiO_4 melt and the density of Fe-bearing silicate melts from 0 to 161 GPa. *Journal of Geophysical Research*, *117*, 1–19. https://doi.org/10.1029/2012JB009403

Thorne, M. S., Lay, T., Garnero, E. J., Jahnke, G., & Igel, H. (2007). Seismic imaging of the laterally varying D″ region beneath the cocos plate. *Geophysical Journal International*, *170*, 635–648. https://doi.org/10.1111/j.1365-246X.2006.03279.x

Trønnes, R. G. (2010). Structure, mineralogy, and dynamics of the lowermost mantle. *Mineralogy and Petrology*, *99*, 243–261. https://doi.org/10.1007/s00710-009-0068-z

Tsuchiya, T., & Tsuchiya, J. (2006). Effect of impurity on the elasticity of perovskite and postperovskite: Velocity contrast across the postperovskite transition in (Mg, Fe, Al)(Si, Al)O_3. *Geophysical Research Letters*, *33*, L12S04. https://doi.org/10.1029/2006gl025706

Tsuchiya, T., Tsuchiya, J., Umemoto, K., & Wentzcovitch, R. (2004). Phase transition in $MgSiO_3$ perovskite in the Earth's lower mantle. *Earth and Planetary Science Letters*, *224*, 241–248. https://doi.org/10.1016/j.epsl.2004.05.017

Vilella, K., Bodin, T., Boukaré, C. E., Deschamps, F., Badro, J., Ballmer, M. D., & Li, Y. (2021). Constraints on the composition and temperature of LLSVPs from seismic properties of lower mantle minerals. *Earth and Planetary Science Letters*, *554*. https://doi.org/10.1016/j.epsl.2020.116685

Weber, M. (1993). *P* wave and *S* wave reflections from anomalies in the lowermost mantle. *Geophysical Journal International*, *115*, 183–210.

Wentzcovitch, R. M., Tsuchiya, T., & Tsuchiya, J. (2006). $MgSiO_3$ postperovskite at D″ conditions. *Proceedings of the National Academy of Sciences of the United States of America*, *103*, 543–546. https://doi.org/10.1073/pnas.0506879103

Wessel, P., & Smith, W. H. F. (1995). *New version of the generic mapping tools released, EOS transact* (Vol. 76, p. 329). American Geophysical Union. https://doi.org/10.1029/95eo00198

Williams, Q., & Garnero, E. J. (1996). Seismic evidence for partial melt at the base of Earth's mantle. *Science*, *273*, 1528–1530. https://doi.org/10.1126/science.273.5281.1528

Wookey, J., Stackhouse, S., Kendall, J. M., Brodholt, J. P., & Price, G. D. (2005). Efficacy of the post-perovskite phase as an explanation of lowermost mantle seismic properties. *Nature*, *438*, 1004–1008. https://doi.org/10.1038/nature04345

Wysession, M. E., Lay, T., Revenaugh, J., Williams, Q., Garnero, E. J., Jeanloz, R., et al. (1998). The D" discontinuity and its implications. In M. Gurnis, et al. (Eds.), *The core-mantle boundary region*, *Geodynamics Series* (Vol. 28, pp. 273–297). AGU. https://doi.org/10.1029/GD028p0273

Yang, K., Dong, X., & Zhang, J. (2021). Polarity-reversal correction for vector-based elastic reverse time migration. *Geophysics*, *86*, S45–S58. https://doi.org/10.1190/geo2020-0033.1

Young, C. J., & Lay, T. (1990). Multiple phase-analysis of the shear velocity structure in the D" region beneath Alaska. *J Geophys Res Solid Earth Planets*, *95*. https://doi.org/10.1029/jb095ib11p17385

Yu, S., & Garnero, E. J. (2018). Ultralow velocity zone locations: A global assessment. *Geochemistry, Geophysics, Geosystems*, *19*, 396–414. https://doi.org/10.1002/2017GC007281

Zoeppritz, K. (1919). Über reflexion und Durchgang seismischer Wellen durch Unstetigkeitsflächen (pp. 66–84). Göttinger Nachrichten.